

Latitudinal divergence in runoff responses to global forestation due to forest-atmosphere feedbacks

Received: 4 July 2025

Accepted: 17 January 2026

Published online: 09 February 2026

 Check for updates

Fei Kan¹, Xu Lian¹✉, Hao Xu¹, Shuchang Tang¹, Jiangpeng Cui²,
Chris Huntingford³, Mingze Sun¹, Xichen Li⁴ & Shilong Piao¹✉

Forestation is a pivotal nature-based solution for mitigating global warming, yet its unintended hydrological outcomes and associated geospatial patterns remain understudied. Here, we combine land-atmosphere coupled models with the Budyko framework to show that forest-atmosphere feedbacks dominate a latitudinal divergence in runoff responses induced by global potential forestation, with increases in tropical regions but declines in boreal regions. In tropical regions, substantial precipitation gains due to intensified upward moisture transport overwhelm the negative effects of forest-driven evapotranspiration (ET) enhancement. Conversely, in boreal regions, limited precipitation gains are insufficient to offset enhanced evaporative loss, driven by increased atmospheric demand due to elevated surface net radiation. The negative effects of direct forest expansion vary along the dryness gradient, with peak impacts in energy-water transitional regions. Our study highlights the necessity to incorporate hydrological considerations into carbon- or temperature-focused afforestation planning, and caution afforestation at high-latitudes where new forests may exacerbate water scarcity.

Forestation—including afforestation, reforestation and forest management—has been advocated as a cost-effective nature-based strategy to curb climate change by sequestering atmospheric CO₂ (refs. 1–5). To optimize the climate benefits of forestation, strategic tree planting in suitable locations is essential. Previous studies indicate that, when moving from tropical to boreal regions, not only does the carbon sequestration potential of forests decline, but the biophysical effects also shift from cooling to warming mainly due to a darkening of tree canopies, cautioning the limited climate benefits of afforestation in boreal regions^{6–10}. Such insights, however, rarely consider potential outcomes of forestation on the local hydrological cycle, particularly changes in freshwater availability through alteration to runoff. Recently, an expanding body of literature has demonstrated that ecological restoration projects have caused a significant decline in land

water availability due to increased water consumption through evapotranspiration (ET) by planted trees^{11,12}. The forest-driven exacerbation of freshwater availability poses a prominent threat to sustainable development of human society, particularly in dry regions where water resources are inherently scarce^{13–15}.

Forests, compared to short vegetation they replace, often exhibit higher ET rates because of their distinct functional traits and canopy boundary-layer characteristics. These include deeper roots that can access subsurface water reserves, denser canopy that enhances both transpiration and rainfall interception, lower surface albedo that increases available solar energy for ET, and lower aerodynamic resistance that facilitates stronger turbulent transfer^{8,16–18}. Previous assessments of the hydrological consequences of forest change have largely relied upon data from paired-watershed experiments (PWE)^{19–22}. This

¹Institute of Carbon Neutrality, Sino-French Institute for Earth System Science, College of Urban and Environmental Sciences, Peking University, Beijing, China. ²State Key Laboratory of Tibetan Plateau Earth System and Resources Environment (TPESRE), Institute of Tibetan Plateau Research, Chinese Academy of Sciences, Beijing, China. ³UK Centre for Ecology and Hydrology, Wallingford, Oxfordshire, UK. ⁴Institute of Atmospheric Physics, Chinese Academy of Sciences, Beijing, China. ✉e-mail: xulian@pku.edu.cn; slpiao@pku.edu.cn

approach involved a comparison between two adjacent catchments that have similar characteristics over a prolonged period, except that one catchment has undergone major land cover changes while the other remains unchanged²³. Most PWE-based studies demonstrated that small-scale (i.e., catchment-level) afforestation leads to a decrease in surface runoff and soil moisture owing to the enhanced evaporative demand of growing trees^{19,21,22,24,25}. The runoff-suppressing effect of afforestation was also supported by analyses based on the Budyko framework, which also offers an empirical approach for attributing observed runoff changes into contributions from local atmospheric changes (i.e., altered precipitation and potential evapotranspiration, PET) and vegetation cover changes^{26,27}. A key underlying assumption of these studies is that atmospheric conditions, particularly precipitation, were independent of vegetation changes. However, more recent studies have reported opposing results for larger catchments, showing either minimal impact^{28,29} or even increased surface water yields due to forest expansion^{30,31}. These apparent inconsistencies in the hydrological effects of forests may arise from potential rainfall feedbacks that become significant only for larger spatial scales of increased tree cover³².

Recently, observational studies have increasingly recognized that vegetation-driven ET can promote downwind precipitation through atmospheric moisture transport and recycling^{33–37}. Although moisture-tracking models, which can effectively depict the teleconnections between moisture source (ET) and sink (precipitation), are capable of quantifying the impact of forestation on precipitation and subsequently runoff through recycling of evaporated moisture, this approach intrinsically overlooks the potential additional moisture imported from oceans due to reorganizations in atmospheric circulation patterns³⁸. Coupled Earth system models (ESMs) enable more comprehensive assessment of afforestation's hydrological impacts by simultaneously accounting for direct recycling of evaporated moisture and alterations in atmospheric circulation patterns. Model-based studies suggest that forest changes, from regional to global scales, affect precipitation locally, and also remotely through synoptic-scale atmospheric anomalies (e.g., cyclone) or large-scale circulation shifts^{39–44}. Most existing modelling studies focus on the feedbacks of deforestation^{41,43,45,46}. However, given that the hydrological responses to afforestation and deforestation are asymmetric and that the regions suitable for potential afforestation are largely distinct from historically deforested areas^{44,47,48}, it remains essential to investigate the hydrological consequences of afforestation. In addition, these simulations predominantly rely on idealized (e.g., 100% or 50%) or historical afforestation/deforestation scenarios^{44,49,50}. Such scenarios fail to account for current and local-specific climate constraints on achievable forestation potential^{6,44,50}, thus potentially limiting their applicability in guiding science-based strategies for future afforestation initiatives.

Beyond altering precipitation, forestation also modifies near-surface meteorological conditions (e.g., surface net radiation, temperature, and humidity)¹⁶, which influence atmospheric water demand by regulating PET, thereby affecting the partitioning of precipitation into runoff versus ET. Although the influence of PET changes is often considered secondary to that of precipitation, it can become more pronounced in energy-limited high-latitude regions⁴⁵. This is because the transition from snow-covered surfaces to darker forests substantially increases surface net radiation^{10,51}, which enhances PET and thus suppresses runoff generation. Conversely, in tropical regions where the atmosphere is more convectively unstable and oceanic moisture supply is abundant^{52–54}, high rates of moisture recycling over rainforests amplify precipitation responses to forest expansion^{36,55}. For example, previous modeling studies have suggested that large-scale afforestation enhances precipitation more substantially in the tropics than in boreal regions^{44,49}. These coexisting and counteracting mechanisms imply the balance between effects of precipitation and

PET may vary geographically. So far, it remains unknown about the net effect of forest-atmosphere feedbacks on runoff, and the overall hydrological impact that further incorporates the direct forest-driven ET increase. These knowledge gaps motivate us to provide a more comprehensive quantification of runoff responses that account for the complex interplay between precipitation, PET, and ET, which can complement current afforestation policies that predominantly emphasize carbon sequestration or temperature modulation^{7,8}.

We here used a coupled land-atmosphere model—the Institute Pierre Simon Laplace climate model (IPSL-CM)^{56,57}—to characterise the potential hydrological outcomes of global forestation. To better inform the implications of global forestation strategies, as proposed to achieve “Net Zero” targets, we applied a full-potential forestation scenario using the Bastin et al.'s dataset (Bastin_Full), in which trees will be planted to the maximum potential of land carrying capacity⁵⁸ (Supplementary Fig. 1). Two equilibrium simulations were performed, prescribed identically with a fixed atmospheric CO₂ concentration of 400 ppm (i.e., close to mean CO₂ concentration over 2011–2020), and with the same boundary conditions of sea surface temperature (SST) and sea ice concentrations (SIC) at 400 ppm (Methods). The forestation experiment (SCE) is forced by the full-potential tree restoration map predicted by a machine-learning approach⁵⁸, and the control experiment (CTL) is forced by current land cover map⁵⁹. The difference between SCE and CTL determines all biophysical effects of global potential forestation on runoff. We then applied the Budyko framework^{26,60,61} to further disaggregate runoff changes into the contribution from direct forest cover increase and forest-atmosphere feedbacks (i.e., changes in precipitation and PET).

Results

Hydrological effects of global potential forestation

We first quantified the hydrological footprint of global tree planting by comparing our two coupled simulations forced by full-potential and current tree cover maps (Fig. 1). At the global scale, full-potential forestation is estimated to increase terrestrial ET by 5.3% (Fig. 1e). The enhancement of ET is found over 70.3% of the land surface, and as expected, with the strongest increase occurring in regions with the highest afforestation potential (Fig. 1a and Supplementary Fig. 2a). The vegetation-driven ET increases are primarily attributed to enhanced canopy transpiration and interception, partially offset by reduced soil evaporation (Supplementary Fig. 3). Forestation-induced ET increase drives an intensification of the terrestrial water cycle by both enhancing the amount of terrestrial water vapour released to the atmosphere and also promoting turbulent and convective activities within the atmospheric boundary layer⁶². Our simulations exhibit that precipitation generally increases in response to forest expansion (Fig. 1b and Supplementary Fig. 2b), which is approximately a 4.2% increase of global mean precipitation (Fig. 1e). However, compared to ET changes, the magnitudes and even signs of rainfall responses show stronger spatial variability, demonstrating that the recycling of evaporated moisture by rainfall is more complex than simply returning the moisture at the same location. Precipitation increases markedly in tropical and subtropical regions and in temperate wet regions, whereas in boreal regions it shows only slight increases or even decreases (Fig. 1b and Supplementary Fig. 2b). This spatial pattern is broadly consistent with the observed sensitivity of precipitation to vegetation^{33,63}.

The spatial mismatch between water source (ET) and water sink (precipitation) reshapes surface water availability. We find that precipitation changes are insufficient to compensate for the soil moisture loss induced by enhanced ET for most vegetated surfaces. Consequently, soil moisture depletion occurs across 66.9% of land area (Fig. 1c), causing a 2.7% decline in global mean soil moisture (Fig. 1e). To understand the influence of global forestation on freshwater availability, we specifically focus on analyzing runoff responses (Fig. 1d). Our simulations show that, globally, full-potential forestation

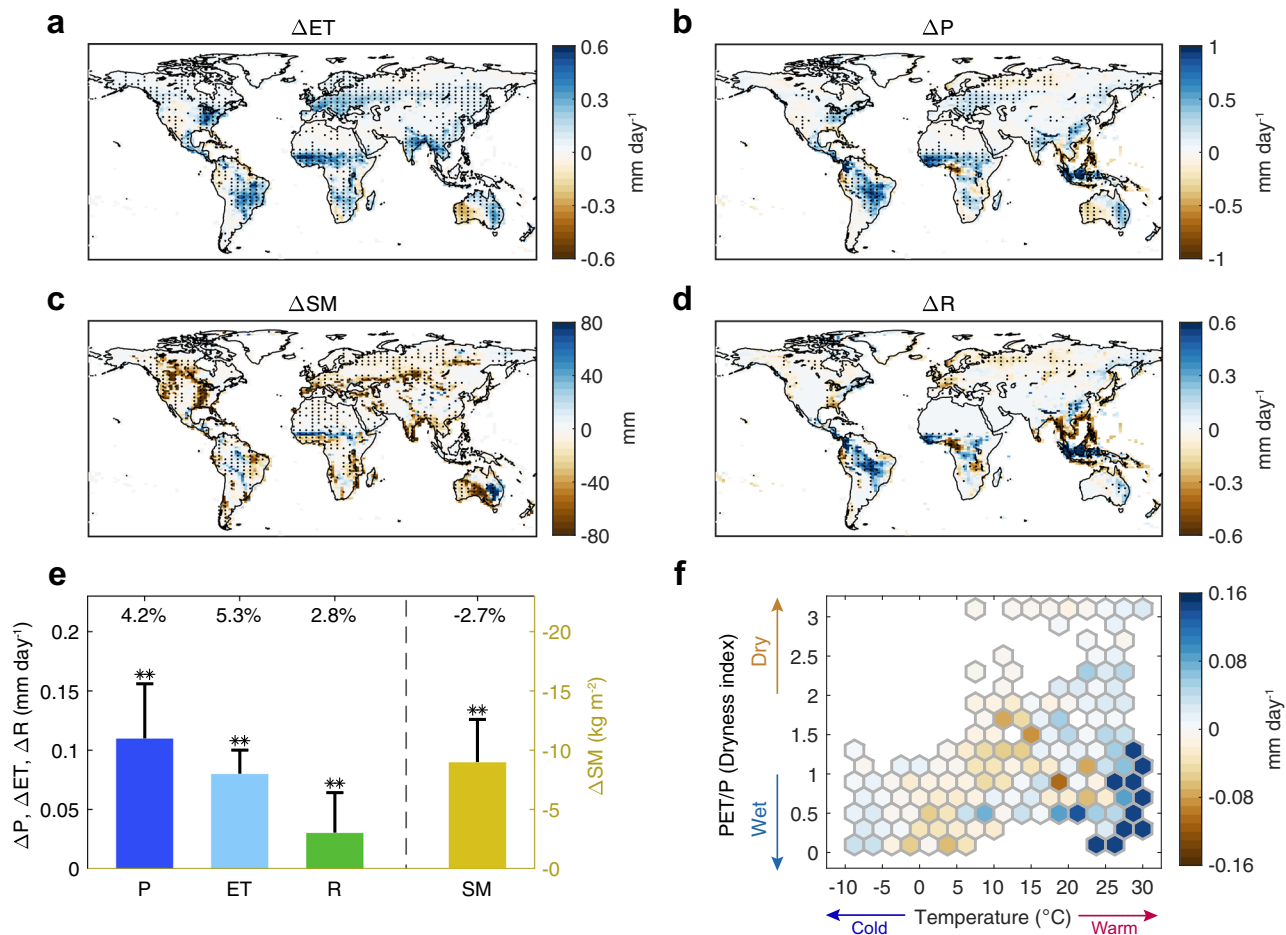


Fig. 1 | Model-estimated impacts of global potential forestation on the hydrological cycle. a–d Geographical patterns of the last 60-year mean changes in annual evapotranspiration (ΔET), precipitation (ΔP), soil moisture (ΔSM) and surface runoff (ΔR) due to global potential forestation. Shown are values from the Bastin_Full simulation minus the CTL simulation. Black stipples in these panels denote statistically significant change using the paired sample *t*-test at the 5% significance level. **e** Global annual mean of forestation-induced changes in P, ET, R and

SM, with error bars indicating the 1-standard deviation of the last 60-year series. ** $p < 0.05$; * $p < 0.1$. Numbers at the panel top show the percentage change in the corresponding variable. Under equilibrium conditions, runoff changes equal precipitation changes minus ET changes ($\Delta R = \Delta P - \Delta ET$). **f** Distribution of ΔR in the space of annual mean temperature and dryness index (the ratio of potential evapotranspiration to precipitation, PET/P) in CTL. The potential evapotranspiration (PET) value is the mean estimates of the two Penman-based PET algorithms.

could lead to a significant increase in annual average runoff by 2.8%, suggesting that global forestation overall increases surface freshwater availability (Fig. 1e). This global value is relatively small due to the spatial compensation between regions with wetting (increased runoff) and drying (decreased runoff) trends. At the local scale, forestation could induce pronounced runoff changes (Supplementary Fig. 4a), with magnitudes ranging from 3.7% to 21.4% in most regions (corresponding to the 25th and 75th percentiles; Supplementary Fig. 4b). Notably, in some arid and semi-arid regions, such as Central Asia, the Sahel, South Africa, and Australia, although forestation causes small absolute runoff changes ($< 0.1 \text{ mm day}^{-1}$), the relative changes can exceed 50% due to the low background runoff (Supplementary Fig. 4a).

Our analysis reveals that regional runoff responses depend tightly on the local climatic conditions, exhibiting greater spatial heterogeneity than ET and precipitation changes (Fig. 1d, f). In general, runoff exhibits divergent responses across latitudinal (or thermal) gradients, with increased runoff generally clustered in warm tropical and temperate regions, but decreased runoff mainly located in cold boreal areas. In most monsoon-controlled tropical or subtropical regions, including the Brazil, Sahel, the Congo Basin, southern Africa, southeastern China, Indonesia and northeastern Australia, precipitation increases frequently override concurrent increases in ET caused by extra forest cover and thereby result in increases in runoff (Fig. 1a, b,

d). This runoff increase, driven by increase of precipitation exceeding that of ET, is also detected in some extremely cold regions, such as northeastern Siberia. In the Northern Hemisphere mid-to-high latitudes, particularly in Europe, Russia, and eastern North America, there is instead a reduction of runoff mainly because the increased precipitation cannot fully compensate for the enhanced ET (Fig. 1a, b, d). However, in northern Russia, the concurrent reduction in precipitation combined with the increased ET further amplifies the runoff decline (Fig. 1a, b, d). It is worth noting that the projected runoff decrease due to global forestation is also detected in some tropical regions, mainly clustered in South Asia and the Congo basin (Fig. 1a, b, d).

Since the idealised full-potential afforestation scenario (Bastin_Full) may overestimate the actual reforestation potential^{64–66}, we further incorporated additional constraints on the potential forestation maps to test the robustness of results. Building on Bastin_Full, a new scenario (Bastin_Refined_Climate) additionally excludes areas with frequent fire occurrences or with expected albedo-induced regional warming after afforestation, and another new scenario (Bastin_Refined_Climate&Land) further excludes croplands, built-up lands, and wetlands. Our simulations forced by refined potential forestation maps produced a latitudinal gradient of runoff responses similar to that of Bastin_Full, though with regional difference in the hydrological effects (Supplementary Fig. 5). Compared with Bastin_Full, reduced

forestation area over tropical grasslands and savannas leads to less strong tropical runoff increase; and further exclusion of afforestation over croplands and urban areas in Bastin_Refined_Climate&Land show less significant decreases in high-latitude regions and weaker increases in low-latitude regions. (Supplementary Figs. 1 and 5). In both afforestation scenarios, the contrasting pattern of enhanced tropical runoff and suppressed high-latitude runoff remains evident.

To further verify our simulated latitudinal gradient of runoff responses to forestation, we calculated the observed sensitivity of precipitation minus ET (P–ET) to forest cover changes based on spatial regression, and retained grid cells where precipitation and ET both exhibit significant sensitivity to forest cover changes (Methods). Over multi-decadal timescales, P–ET serves as an approximate estimate for runoff. This observation-based analysis shows a clear latitudinal contrast: P–ET overall decreases with forest cover gain in high-latitude regions but increases in the tropics (Supplementary Fig. 6), in agreement with our model-based findings. Our results are also corroborated by previous model-based assessments of global forestation effects on the hydrological cycle. For example, De Hertog et al.⁴⁹ and Portmann et al.⁴⁴ consistently show a clear latitudinal gradient, with precipitation generally increasing in the tropics and decreasing or showing weaker changes at higher latitudes, in line with our findings.

Forest-atmosphere feedbacks driving the latitudinal contrast

Considering that ET is affected by both direct vegetation cover changes and indirect atmospheric changes (precipitation and near-surface meteorology as described by PET), we provide a quantitative assessment of the separate roles of land surface changes (ΔR_{land}) and forest-atmosphere feedbacks (ΔR_{atm}) in the forestation-induced runoff changes, based on the Budyko framework^{45,61} (Methods). This framework characterizes land surface controls on runoff using a region-specific parameter n , which represents the ability of a watershed or region to retain precipitated water for ET. Higher values of n indicate a greater partitioning of available precipitation toward ET rather than runoff. The impacts of altered surface parameter n on runoff (ΔR_{land}) refer to the runoff changes caused by terrestrial ET alterations under conditions of unchanged precipitation and PET. Forest-atmosphere feedbacks on runoff are further decomposed into contributions from precipitation (ΔR_P) and PET (ΔR_{PET}) changes. Here, we mainly employed two commonly used variants of the Penman equation for PET estimation: the open-water Penman equation (Penman-OW)⁶⁷ and the reference crop Penman-Monteith equation (PM-RC)⁶⁸ (Methods).

Our key finding is that the divergent runoff responses to forestation between tropical and boreal regions, as shown in Fig. 1d, f, are driven by forest-atmosphere feedbacks (ΔR_{atm} ; Fig. 2a, b), rather than by direct land cover changes (ΔR_{land}). Compared to ΔR_{land} that show globally consistently negative effects and particularly in mid-to-low latitudes (Fig. 2c, d), the dominant forest-atmosphere feedbacks produce opposite responses along latitudinal gradients: widespread runoff reductions in northern high latitudes (e.g., Eurasia), whereas runoff enhancements in mid-to-low latitudes (e.g., the Brazil, Africa, South-east Asia and southern Europe) (Fig. 2a, b). Furthermore, the two further constrained forestation scenarios consistently show that forest-atmosphere feedbacks strongly shape the latitudinal gradient of runoff responses (Supplementary Fig. 7).

While the Budyko-based attribution highlights the dominant role of forest-atmosphere feedbacks in driving runoff responses, it does not explicitly account for the influence of altered precipitation characteristics, such as rainfall intensity and snow fraction, on runoff generation processes⁶⁹. To address this potential bias, we adopted a modified approach following Zhou et al.⁶¹, which isolates the effects of altered precipitation characteristics and incorporates these into atmospheric feedbacks (Methods). The results from this modified method align well with our main findings, confirming that forest-atmosphere feedbacks predominantly drive the latitudinal divergence

of forestation-induced runoff changes (Supplementary Fig. 8). In addition, we assessed how inter-decadal to multi-decadal climate variability influences the attribution results by varying time windows of the equilibrium simulations based on a bootstrap approach (Methods). The latitudinal pattern of runoff responses and the leading role of forest-atmosphere feedbacks are consistent across all time windows, indicating negligible influence of internal climate variability on our results (Supplementary Fig. 9). Furthermore, applying alternative PET estimation methods – including two Penman-based equations and another energy-balance approach – generates highly consistent results, further strengthening the reliability of our findings (Methods, Supplementary Fig. 10).

By analyzing the runoff changes within the temperate-dryness space, we find that the overall runoff responses due to forest-atmosphere feedbacks are more dependent on background temperature than dryness conditions (Fig. 2b). Therefore, we quantified the hydrological responses of forestation in warm regions (with annual mean temperature > 12.5 °C) versus in cold regions (< 12.5 °C) (Supplementary Fig. 11). Given that mean runoff differs by several-fold between warm and cold regions, we used relative rather than absolute changes in our subsequent analysis to facilitate comparison of forestation-induced hydrological responses. We find that forest-atmosphere feedbacks generate a substantial 6.6% runoff increase in warm regions, but the increase in cold regions is much smaller at just 1.3% (Fig. 3c).

Separate roles of precipitation and PET changes

Further decomposition of ΔR_{atm} into ΔR_P and ΔR_{PET} reveals that forestation-induced precipitation and PET changes both contribute significantly to the latitudinal divergence of runoff responses (Fig. 3 and Supplementary Fig. 12). As forestation-induced precipitation changes shift from strong increases in tropics to modest increases or even slight declines at high latitudes (Fig. 1b), the resultant ΔR_P exhibits a similar spatial pattern of precipitation responses (Fig. 3a and Supplementary Fig. 12a). Compared to precipitation, PET demonstrates opposite signs of effects on runoff across latitudinal gradients: PET decreases drive modest runoff increases at mid-to-low latitudes, whereas PET increases drive strong runoff reductions in high latitudes (Fig. 3b, Supplementary Figs. 12b and 13a, c). In warm regions, precipitation changes lead to a strong runoff increase (+6.4%), which is slightly amplified by a modest PET-driven runoff rise (+0.2%) (Fig. 3c). The precipitation-driven runoff increments are most prominent in some monsoon regions, with values exceeding 40% (Supplementary Fig. 4e). Conversely, in cold regions, the PET-driven runoff reduction (–2.0%) becomes non-negligible, largely offsetting the precipitation-driven increase (+3.3%) (Fig. 3c). At some locations, forestation-driven PET changes could reduce runoff by over 20% (Supplementary Fig. 4f).

We next explore the physical mechanisms underlying the spatial variability of precipitation and PET responses to forestation. By aggregating the grid-level changes to regional scale, we find that precipitation significantly increases in both warm and cold regions (Fig. 3d). However, the magnitude of precipitation increment in cold regions is only about one-third of that in warm regions (Fig. 3d). We further decompose precipitation change into the contribution from four physical processes alterations: thermodynamic effects associated with atmospheric water vapour (ΔWV), vertical moisture transport ($\Delta Vert$), horizontal moisture advection (ΔAdv), and terrestrial ET (ΔET)^{70–73}. The residual term (Res) representing differences between modelled precipitation changes and the sum of all processes. Our analysis shows that, local ET enhancements contribute comparably to precipitation enhancement in both warm and cold regions, and thus cannot explain the asymmetric precipitation enhancement in warm versus cold regions (Fig. 3d). Instead, atmospheric dynamics and thermodynamics are responsible for the latitudinally asymmetric precipitation changes (Fig. 3d and Supplementary Fig. 14).

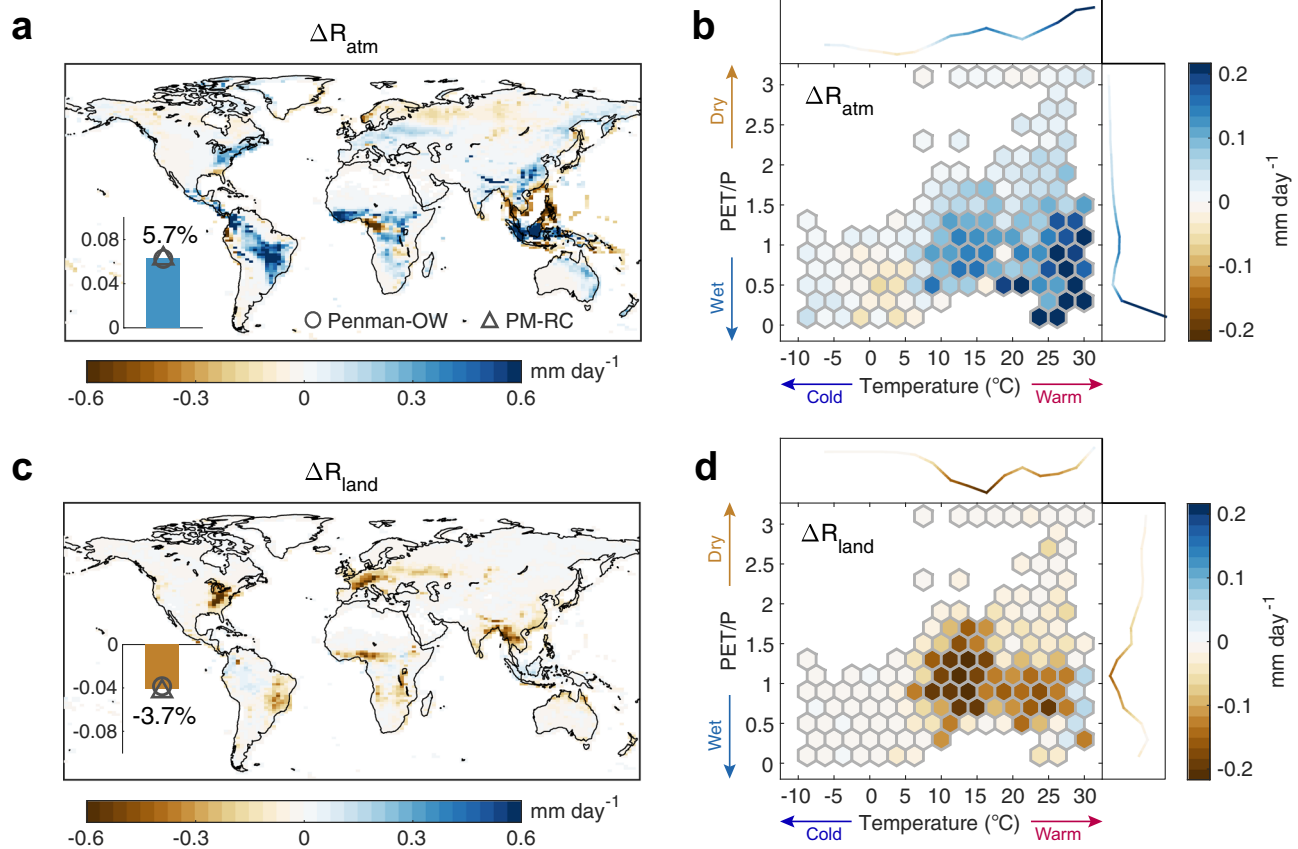


Fig. 2 | Runoff changes caused by indirect forest-atmosphere feedbacks and direct land surface effects of global potential forestation. a, c Geographical patterns of runoff changes associated with forest-atmosphere feedbacks (ΔR_{atm} ; **a**) and land surface changes (ΔR_{land} ; **c**) respectively. Shown are the mean results of the two Penman-based PET algorithms. The insets display the bar plots of global mean of ΔR_{atm} and ΔR_{land} based on the mean result of two PET estimates, respectively.

Estimates by Penman-OW and PM-RC are shown as circles and triangles, respectively. Numbers show the percent change in runoff relative to CTL-simulated runoff. **b, d** Distribution of ΔR_{atm} (**b**) and ΔR_{land} (**d**) in the space of annual mean temperature and dryness index (PET/P) in CTL. Marginal curves indicate the partial dependence of the ΔR_{atm} or ΔR_{land} on temperature (top) and PET/P (right). The PET value is the mean estimates of the two Penman-based PET algorithms.

In warm regions, forestation-induced precipitation increases are primarily contributed by $\Delta Vert$ (Fig. 3d and Supplementary Fig. 14c). This is because forestation significantly enhances the Convective Available Potential Energy (CAPE) and the vertical gradient of specific humidity (Supplementary Fig. 15a, b), indicative of reduced atmospheric stability, thereby promoting the upward motion of moisture (Supplementary Fig. 15c) and increasing convective precipitation (Supplementary Fig. 14c). The changes in vertical velocity throughout the troposphere are intrinsically linked to forestation-induced alterations in atmospheric circulation and moisture convergence (Supplementary Fig. 15c). This precipitation increase is further amplified by ΔAdv (Fig. 3d), due to enhanced horizontal advection of moisture from upwind regions (Supplementary Fig. 15c). For example, the southeasterly winds over Southeast China are strengthened, enhancing moisture transport from the ocean and consequently favoring advective rainfall in that region (Supplementary Figs. 14b and 15c). The dominance of dynamic processes ($\Delta Vert + \Delta Adv$) is particularly evident in monsoon-affected regions, including South America, Africa, East Asia (Supplementary Fig. 14b, c). This suggests that large-scale sea breeze circulations, as perturbed by global forestation, tend to converge more ocean-sourced moisture, thereby enhancing regional precipitation recycling. In addition, the effects of thermodynamic processes, ΔWV , are also non-negligible in warm regions (Fig. 3d and Supplementary Fig. 14a). The residual components also exhibit a precipitation reduction in warm regions, particularly in southeastern China (Fig. 3d and Supplementary

Fig. 14e), which may be related to weakened transient eddies (storm systems)⁷⁴.

In cold regions, while global forestation also causes reorganizations of atmospheric circulation patterns (Supplementary Fig. 15), the circulation-induced precipitation changes are insignificant regionally because the positive and negative effects spatially offset each other (Fig. 3d and Supplementary Fig. 14b, c). However, at local scales, the circulation-induced impacts on precipitation remain substantial. For example, over Eurasia, the marked reduction in CAPE suppresses upward air motion and consequently weakens convective precipitation (Supplementary Figs. 14c and 15). In addition, the large anticyclonic anomaly induced by forestation over Eurasia weakens the prevailing westerlies, thereby reducing moisture advection from the North Atlantic and inhibiting advective precipitation. (Supplementary Figs. 14b and 15c). Beyond such effects of dynamic processes, thermodynamic processes associated with changes in atmospheric water vapor (ΔWV) further contribute to an insignificant precipitation reduction in cold regions, particularly over Europe and western North America (Fig. 3d and Supplementary Fig. 14a).

Apart from precipitation changes, forestation also triggers asymmetric responses in PET, with warm regions showing a 0.7% ($\pm 0.6\%$) decrease and cold regions a 1.0% ($\pm 2.0\%$) increase (Fig. 3e and Supplementary Fig. 13a, c). These contrast PET responses arise primarily from the trade-off between alterations in surface available energy ($R_n - G$, representing the surface energy constraint) and atmospheric aridity (indicated by vapor pressure deficit, VPD) (Fig. 3e and

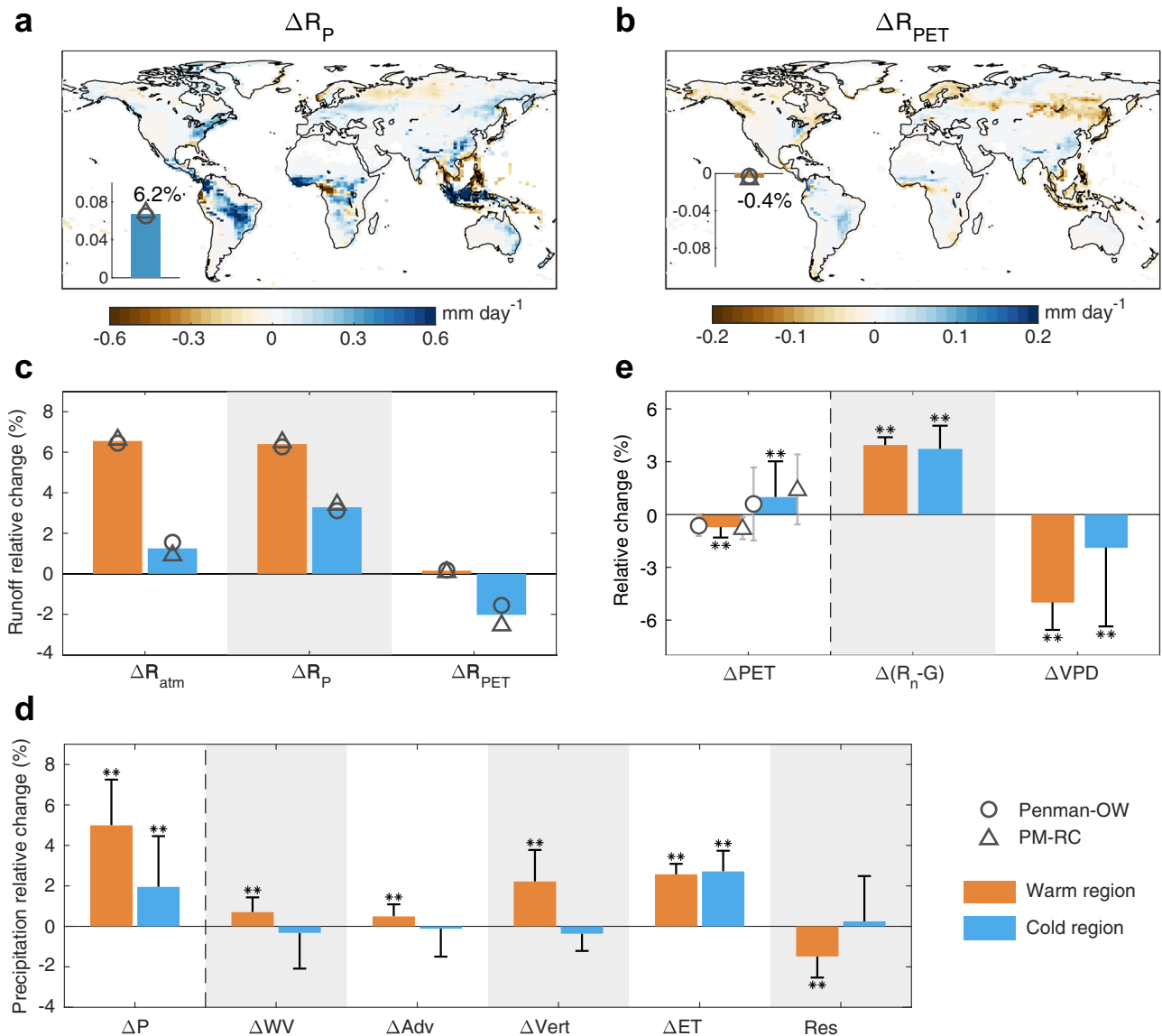


Fig. 3 | Regional mechanisms underlying the latitudinal divergence in runoff responses due to forest-atmosphere feedbacks of forestation. **a**, **b** Geographical patterns of runoff changes associated with precipitation changes (ΔR_p ; **a**) and PET changes (ΔR_{PET} ; **b**), respectively. Shown are the mean results of the two Penman-based PET algorithms. The insets display the bar plots of global mean of ΔR_p and ΔR_{PET} based on the mean result of two PET methods, respectively. Numbers show the percent change in runoff relative to CTL-simulated runoff. **c** Regional annual mean of runoff relative changes due to forest-atmosphere feedbacks (ΔR_{atm}), precipitation changes (ΔR_p) and PET changes (ΔR_{PET}) in both warm ($> 12.5^\circ\text{C}$) and cold ($< 12.5^\circ\text{C}$) regions. The bar plots are the mean results of the two Penman-based PET algorithms. **d** Regional components of precipitation relative changes associated with four physical processes in both warm and cold regions. The four main

processes are thermodynamic effect (ΔWV), altered horizontal advection (ΔAdv), altered vertical transport ($\Delta Vert$) and land ET changes (ΔET). The residual (Res) represents differences between precipitation changes (ΔP) and the combined contribution from the four processes, reflecting the impacts of transient eddies. **e** Regional annual mean of forestation-induced relative changes in PET (ΔPET), and relative changes in its two main drivers, including surface available energy ($\Delta(R_n - G)$), atmospheric vapour pressure deficit (ΔVPD), respectively. The bar plots of ΔPET are the mean results of two Penman-based PET algorithms. Estimates by Penman-OW and PM-RC in (**a–c**) and (**e**) are shown as circles and triangles, respectively. Error bars in (**d**) and (**e**) indicate the 1-standard deviation of the last 60-year series. ** $p < 0.05$; * $p < 0.1$.

Supplementary Fig. 16). Forestation tend to increase $R_n - G$ by lowering surface albedo, but this is insufficient to explain the latitudinal asymmetric PET responses because of the comparable magnitudes of radiation gains between warm and cold regions (warm: +4.0%; cold: +3.7%). Furthermore, forestation tends to reduce VPD, with a greater reduction detected in warm regions (−5.0%) compared to cold regions (−1.9%), suggesting VPD as the primary driver of asymmetric PET responses. By disentangling temperature and humidity contributions to VPD changes (Supplementary Text 1), we demonstrate that forestation leads to larger VPD reductions in warm regions due to stronger cooling and greater humidity increases, whereas in cold regions, the

warming induced by forestation partially counteracts the humidity-driven decline in VPD, resulting in a smaller net decrease (Supplementary Fig. 17). Consequently, the negative effects of reduced VPD are sufficient to counterbalance the positive effects of increased net radiation in warm regions, but not in cold regions, resulting in a PET decrease in warm regions but a PET increase in cold regions (Fig. 3e).

Aridity-level regulation on direct land surface effects

Compared to the circulation-mediated atmospheric feedbacks, direct effects of forest cover increase on runoff (i.e., ΔR_{land}) are more relevant to freshwater availability at the location of tree planting (Fig. 2c, d).

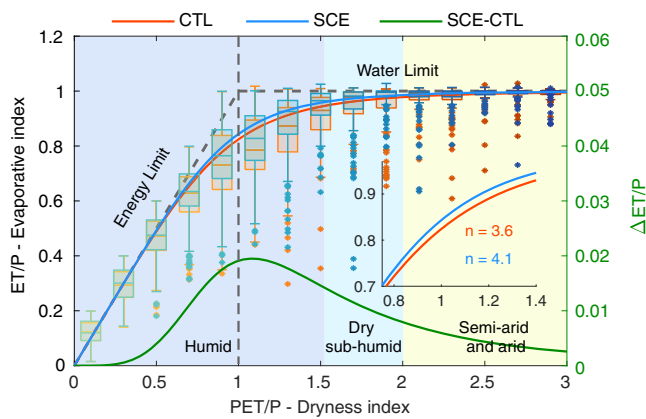


Fig. 4 | Forestation-induced changes in the 60-year mean relationship between dryness index (PET/P) and evaporative index (ET/P). Box plots show the median (horizontal lines), 25th, 75th quartiles, maximum and minimum values (top and bottom of the whiskers), and outliers (dots) of ET/P values determined separately for each 0.2-wide PET/P bin. The solid red and blue lines show the fitted Budyko curves using the global data with the ET/P values falling between 5% and 95% (Supplementary Fig. 18, Method) in CTL (red) and SCE (blue), respectively. The solid green line denotes the difference in the Budyko curves between CTL and SCE. The inset zooms into the transitional regions with P/PET near unity where the two Budyko curves differ the most. The background colors distinguish regions of different dryness levels, that are classified according to the United Nations Environment Programme (UNEP).

Our results reveal that ΔR_{land} could partially offset the ΔR_{atm} -driven runoff increase in tropical regions (e.g., Africa and South America), whereas completely neutralize or even reverse the ΔR_{atm} -driven increase in some temperate zones (e.g., Europe), thereby amplifying the latitudinal divergence in runoff responses (Figs. 1d, f and 2). This more universal negative effect of ΔR_{land} in mid-to-low latitudes are captured by the forestation-induced increase in the surface parameter n (Supplementary Fig. 13b, d), which represents catchment characteristics governing runoff generation and primarily reflects the catchmental water retention capacity^{26,60,75–77}. The consistent increase in n indicates that afforestation-induced catchmental changes overall enhances rainfall partitioning into regional ET, thereby reducing runoff. Along the dryness gradient, the ΔR_{land} -driven runoff decrease exhibits a unimodal pattern, with the most pronounced decrease observed in transitional regions where the P/PET value approaches unity (Fig. 2c, d). In those afforestation hotspots, including Europe, southeastern North America, southern Asia and Africa, the adverse effect of ΔR_{land} could reduce regional runoff by over 40%, far exceeding the global average decline of just 3.7% (Fig. 2c and Supplementary Fig. 4d). These findings are consistent with theories that ET is constrained by water limitations in dry regions and by energy limitations in cold regions^{78,79}.

To better illustrate how background aridity levels affect runoff responses to tree planting, we fitted the Budyko curves – the relationships between the evaporative index (ET/P) and the dryness index (PET/P) – using the global 60-year mean data from both the CTL and SCE scenarios (Fig. 4 and Supplementary Fig. 18, Methods). The shape of curves reflects the global-scale surface characteristic parameter (n). Our results show that potential forestation increases the parameter n from 3.6 in the CTL to 4.1 in the SCE. This indicates a greater partitioning of precipitation towards ET (increased ET/P) driven by enhanced ecosystem water demand from forests, leading to less runoff (decreased R/P, the ratio of runoff to precipitation). Without accounting for precipitation and PET changes, decreased R/P would directly result in runoff yield reduction. The Budyko curves in Fig. 4 illustrate unimodal dependence of ET/P (1-R/P) on the background

dryness, peaking at around PET/P ≈ 1 that represent transitional zones between energy-limited and water-limited regions. The effect of tree planting on the PET/P – ET/P relationship is also robust to the selection of different percentiles used for the fitting of the global Budyko curve (Supplementary Fig. 19).

Discussion

Under current climatic conditions, tree planting up to their maximum potential would, for many locations, accelerate the terrestrial water cycle through enhancing both ET and precipitation, albeit at the expense of reduced surface water resources. By balancing forestation-driven increases in ET and precipitation, our analysis reveals reduced runoff in boreal regions but increased runoff in tropical and temperate regions. We demonstrate that indirect forest-atmosphere feedbacks (due to forest-driven precipitation and PET changes), rather than direct ET enhancement due to forest cover expansion, primarily drive the divergent hydrological responses to afforestation in warm versus cold regions (Fig. 5). In warm regions, particularly humid monsoon zones, global forestation can enhance precipitation substantially mainly by supplying extra moisture to the atmosphere and intensifying vertical moisture transport. Moreover, forestation reduces atmospheric water demand (PET) by decreasing VPD, amplifying the precipitation-dominated runoff increase. Conversely, in cold regions, forestation significantly enhances surface net radiation and thus the energy available for ET (i.e., PET), driving regional runoff declines. The hydrological effect of PET increase largely offsets that of precipitation compensation, thus producing small runoff increases due to forest-atmosphere feedbacks. In contrast to the thermally/latitudinally dependent forest-atmosphere feedbacks, afforestation-induced land surface effect drives spatially consistent runoff suppression along the dryness gradient, reaching maximum intensity in transitional regions where the PET/P value approaches unity. This negative land-surface effect partially counteracts the pronounced runoff increases from forest-atmosphere feedbacks in warm regions, while it overrides the slight runoff increases driven by forest-atmosphere feedbacks in cold regions.

To assess the robustness of our model-based findings, we also performed equilibrium experiments using an independent model, Community Earth System Model (CESM). This model reproduces a similar latitudinal (thermal) pattern of forestation-induced runoff changes, with increases in warm regions and decreases in cold regions, albeit with slightly different magnitudes (Supplementary Fig. 20). Consistent with IPSL-CM, CESM indicates that forest-atmosphere feedbacks predominantly shape the latitudinal gradient of runoff responses (Supplementary Fig. 21). Furthermore, both the water vapor budget analysis for precipitation changes and the attribution of PET changes using net radiation and atmospheric moisture demand corroborate the main conclusions derived from IPSL-CM (Supplementary Fig. 22). For instance, regarding precipitation responses to afforestation, CESM confirms that the pronounced increases in warm regions primarily result from enhanced horizontal and vertical moisture transport driven by circulation adjustments (Supplementary Figs. 22a and 23b, c). Although CESM overall supports the IPSL-based results, some regional discrepancies are notable due to structural and physical differences between the two models. For example, in Southeast Asia, precipitation increases exceed ET increases in IPSL-CM, whereas the opposite pattern is simulated in CESM (Fig. 1 versus Supplementary Fig. 20). Our moisture budget decomposition indicates that this difference stems from contrasting atmospheric circulation responses: IPSL-CM simulates an intensification of convective precipitation, while CESM suggests a suppression (Supplementary Fig. 14c versus Supplementary Fig. 23c). The dominant role of forest-atmosphere feedbacks in shaping runoff responses is further supported by an ensemble of idealized global deforestation simulations

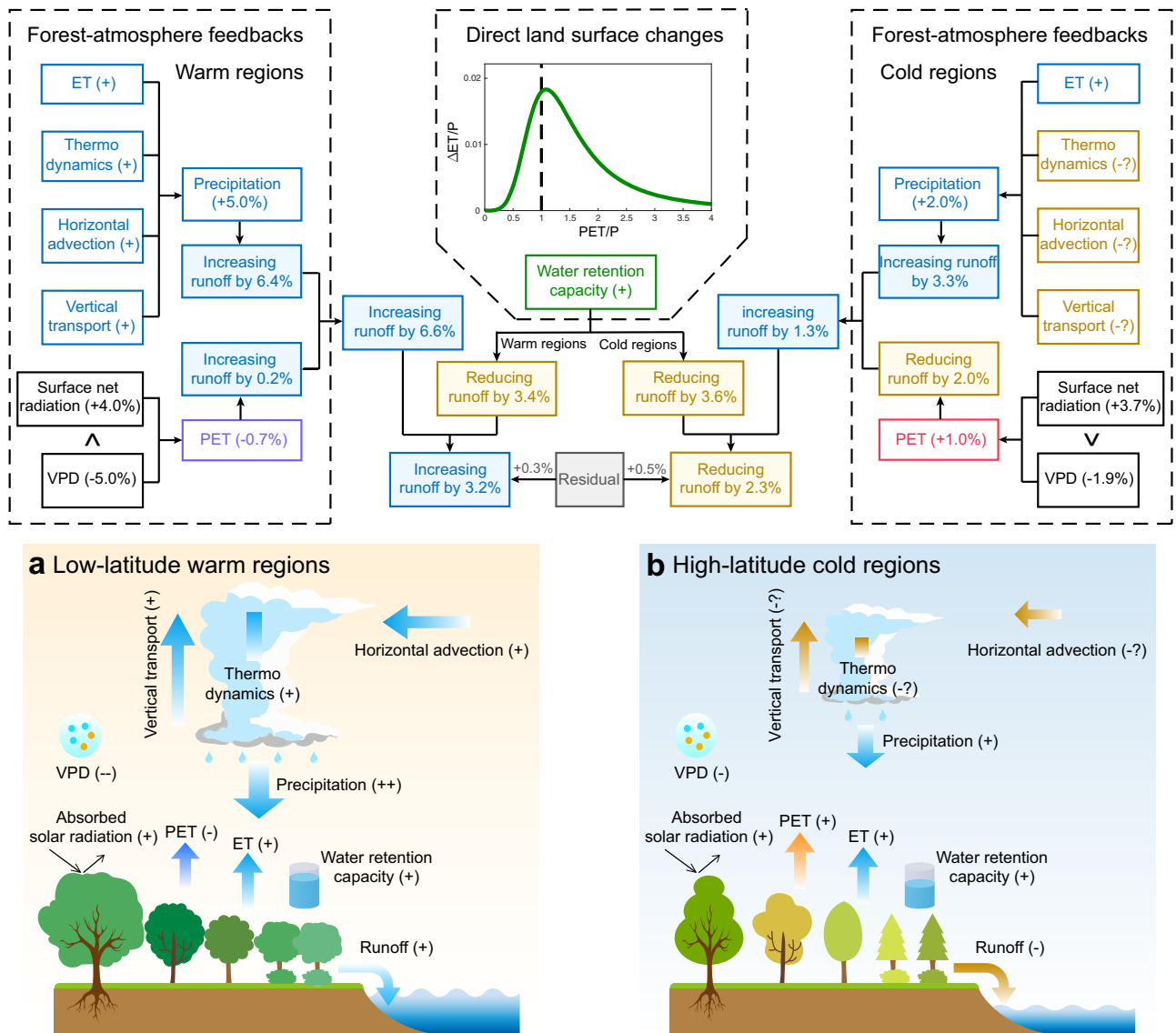


Fig. 5 | Mechanisms of the contrasting runoff responses in warm regions versus cold regions due to global potential forestation. The schematic illustrations and numbers are based on results from IPSL-CM simulations. **a** In low-latitude warm regions, runoff increases because the positive forest-atmosphere feedbacks (increased precipitation and reduced PET) fully compensates for the negative land surface effects (increased water retention capacity). The substantial precipitation increase mainly results from enhanced vertical moisture transport, amplified by horizontal moisture advection, intensified thermodynamic effects and increased ET. The PET decline primarily results from the reduced VPD, whose effect dominates over the increased surface net radiation. **b** In high-latitude cold regions, runoff decreases due to the larger negative land surface effects that override the minor positive effects from forest-atmosphere feedbacks (slightly increased precipitation and largely increased PET). The minimal precipitation increase arises

from ET-driven additional moisture supply counterbalanced by diminished thermodynamic effects and potentially weakened vertical and horizontal moisture transport. The PET rise primarily stems from the dominant role of increased surface net radiation over the reduced VPD. The direct land surface effects of forestation, which are negative in both warm (**a**) and cold (**b**) regions, stems from the increased water retention capacity. This enhanced water retention allows vegetation to allocate precipitation more to ET and less to runoff. This response is most pronounced in areas where PET/P is approximately around 1. The residual term indicates the interactions between forest-atmosphere feedbacks and direct land surface effects. +, positive response to forestation. -, negative response to forestation. The number of + or - denotes the magnitude of the response.?, insignificant response to forestation using Student's t-test at the 5% significance level.

from the Coupled Model Intercomparison Project Phase 6 (CMIP6) Land Use Model Intercomparison Project (LUMIP), in which runoff responses exhibit a similar latitudinal gradient of tropical reductions and mid-to-high latitude increases⁴⁵. Given that hydrological responses to afforestation and deforestation are generally opposite in sign, this opposite pattern under deforestation indirectly corroborates the robustness of our findings.

The latitudinal divergence in forestation-induced runoff responses aligns with an early modeling study on the hydrological effects of historical Earth greening, which also showed increased runoff in the tropics but reductions in Siberia⁸⁰. However, changes of global water

fluxes (in both ET and precipitation) induced by forestation is two to three times larger than that associated with historical greening, indicating that forestation, as a form of non-radiative forcing, can strongly reshape the global hydrological cycle, as consistently highlighted by numerous previous studies⁸¹⁻⁸⁵. These latitudinal gradient in runoff changes have important implications for determining the locations of future afforestation initiatives. Previous research has advocated prioritizing tropical forestation due to their greater carbon sequestration capacity and additional biophysical cooling benefits from enhanced ET⁶⁻⁸. In contrast, boreal afforestation remains contentious due to weaker potential of carbon sinks in conjunction with a net

biophysical warming mainly due to lower albedo of snow-masked canopies^{8,9}. Our findings, from a hydrological perspective, further caution against afforestation practices in boreal regions due to potential reduction of freshwater availability and exacerbation of water stress. Our results also support the hydrological advantages of tropical afforestation, which could enhance water availability to mitigate regional water deficits in some developing countries¹⁵. We therefore highlight the necessity of latitude-specific strategies that simultaneously integrate carbon sequestration, temperature benefits, and hydrological impacts into formulation of afforestation planning.

After balancing runoff increases in tropical/temperate regions and decreases in boreal regions, our model results reveal that global forestation overall enhances global mean runoff. This overall wetting effect contrasts with conventional understanding that afforestation always reduces surface runoff^{19–22}. This perspective, often derived from paired “offline” small-scale catchment studies, is valid only if vegetation changes do not induce detectable modifications in precipitation patterns and near-surface atmospheric conditions. By quantifying the direct hydrological impacts of global forestation (ΔR_{land}) when the forest-atmosphere feedbacks are excluded (Supplementary Text 2), we demonstrate that such assuming no forest-atmosphere feedbacks systematically overestimate the negative effects of afforestation on runoff, with fixed precipitation being the primary source of bias (Supplementary Fig. 24). Therefore, we illustrate that conclusions from small-scale afforestation experiments inadequately represent, or even misrepresent, hydrological outcomes under large-scale implementation, as extensive land cover changes will fundamentally alter moisture advection and trigger substantial precipitation shifts. Since tree planting is a global climate change mitigation strategy (e.g., towards achieving “Net Zero”), we emphasize the necessity to integrate forest-atmosphere feedbacks, particularly precipitation modifications, into the assessments of hydrological responses to large-scale tree planting initiatives.

However, it should be noted that global forestation alters precipitation patterns not merely through a direct recycling of evaporated water from new forests. Moisture tracking analyses that directly prescribe increased ET from new forests are able to isolate the recycling pathway, but inherently neglect circulation-induced moisture convergence. These studies reveal that the majority of evaporated moisture generated locally by tropical potential afforestation would be transported elsewhere and feed precipitation in downwind locations, thereby reducing local water availability^{86,87}. Our findings extend these results by showing that global forestation can also reorganise large-scale atmospheric circulation patterns in tropical regions, drawing more additional moisture from nearby oceans. Previous studies have also demonstrated that vegetation changes in monsoon regions can affect rainfall by perturbing sea-breeze circulations^{41,43,88–92}. This mechanism largely compensates for the evaporated moisture exported downwind, thereby generating net precipitation gains and consequent runoff increases. The alteration in large-scale atmospheric circulation may be associated with forestation-induced changes in surface energy balance, mainly through reduced albedo^{44,51}, which modify the thermal structure of the lower atmosphere and further initiates a stationary Rossby wave train (Supplementary Fig. 25). Therefore, future research of how afforestation affects local water resource availability should accounting for not only increased ET in upwind afforested areas but also reorganized circulation patterns.

While the latitudinally divergent runoff responses to global forestation are robust across both land-atmosphere coupled models examined, there are a few caveats associated with our modeling approach. First, such models lack a dynamic ocean module, thereby ignoring potential impacts of oceanic circulation adjustments on precipitation. Nonetheless, idealized 100% forestation simulations by Portmann et al. using the fully coupled CESM show latitudinal hydrological responses almost consistent with our results⁴⁴. Furthermore, multiple fully coupled models participating in the CMIP6 LUMIP

indicate that idealized large-scale deforestation triggers forest-atmosphere feedbacks with a latitudinal gradient opposite to ours^{45,93}, thereby indirectly corroborating the robustness of our results, given the opposite signs of the biophysical feedbacks between afforestation and deforestation^{44,47,48}. Collectively, these evidences suggest that omitting the teleconnections from oceanic circulations may not qualitatively alter our conclusions unless ocean-mediated feedbacks substantially overpower land-atmosphere coupling effects.

Second, our simulations do not account for the spatial and temporal dynamics of tree rooting depths, which are prescribed as fixed values for each plant functional type (PFT) in land surface models. Hence, the models do not represent how rooting depths vary with hydroclimates, soil properties, topography, and forest age^{94–96}. This simplification may lead to biases, since observations show that the rooting depth tend to increase with aridity to access deeper water sources^{95,96}, and evolve over a tree’s lifetime⁹⁷. For instance, in humid regions like Southeast Asia, using a fixed, potentially overestimated rooting depth for newly planted trees could overestimate the projected increase in ET and the consequent soil water depletion (Fig. 1).

Finally, our global climate models (GCMs) with coarse grid increment are deficient in representing mesoscale feedbacks, but they are capable of capturing the first-order hydroclimatic effects of large-scale forestation. For example, previous modeling studies based on a regional climate model (40-km grid increment)⁹⁰ or a zoomed IPSL-CM have suggested enhanced runoff in response to historical afforestation in China⁴⁰, consistent with our GCM-based results. Nevertheless, GCMs cannot explicitly resolve fine-scale (10–20 km), potentially nonlinear interactions among forest patchiness, convective development, and local precipitation^{98–102}. Therefore, for local-scale afforestation studies, regional climate models (RCMs) with kilometer-scale grid spacing are recommended to better understand the role of mesoscale landscape structure in shaping the local hydrological outcomes of afforestation.

Methods

Equilibrium experiments with coupled land-atmosphere models

In this study, we used the IPSL-CM coupled land-atmosphere climate model to simulate the biophysical effect of global full-potential forestation on runoff under equilibrium climate conditions. IPSL-CM was developed by the Institute Pierre Simon Laplace modeling community with a resolution of $1.26^\circ \times 2.5^\circ$ and has participated in the Coupled Model Intercomparison Project (CMIP) phases 5 and 6 (refs. 56,57). It consists of two major components that have been updated to the latest version: the Laboratoire de Météorologie Dynamique atmospheric general circulation model with zooming capability (LMDZ, version 5, v2076) and the Organising Carbon and Hydrology in Dynamic Ecosystems (ORCHIDEE, v3035) land surface model. LMDZ, featuring 19 vertical layers, characterizes dynamics of atmospheric physical processes such as convection, boundary layer, and cloud^{103,104}, and ORCHIDEE describes water and energy balance, vegetation, and soil carbon cycle in terrestrial ecosystems¹⁰⁵. The ORCHIDEE model divides terrestrial plant function types (PFTs) into 13 categories, including 12 vegetation types and one bare ground type, each with independent parameters to calculate vegetation physiological processes. The IPSL-CM has been widely used to quantify the biophysical impacts of vegetation changes on temperature and the hydrological cycle^{40,106,107}, for its outstanding performance in simulating key vegetation-related processes, including the ratio of vegetation-driven transpiration to the evapotranspiration, T/ET ¹⁰⁸. Model performance was further evaluated using observed streamflow records of 270 screened catchments from the Global Streamflow Indices and Metadata Archive (GSIM)^{109,110} (Supplementary Text 3). The IPSL-CM successfully reproduces cross-catchment runoff variability ($r = 0.66$, $p < 0.01$), with the median of model-observation difference statistically indistinguishable from zero

(Supplementary Fig. 26). This indicates no systematic bias in the IPSL-modelled runoff, supporting the model capability for assessing afforestation-induced runoff responses.

The biophysical impacts of forestation on the hydrological cycle were isolated by a pair of equilibrium experiments. The two experiments differed solely in their prescribed PFT conditions: the “CTL” run was forced with current PFT maps, whereas the “SCE” run was prescribed with the hypothesized PFT maps with global forestation to the full of potential of terrestrial ecosystems. The experiment pair was conducted under the atmospheric CO₂ concentration of 400 ppm. Each equilibrium experiment was run for 100 years. We used the last 60 years of monthly output data for further analysis because the simulations typically reached an equilibrium state in around 40 years, and selecting 60 years also helps reduce the potential influence of inter-decadal and multi-decadal climate variability. Each of the last 60 years could be regarded as an independent run under the equilibrium state, allowing us to estimate the uncertainty in forestation-induced biophysical response.

The current land cover map was derived from the Olson categories, containing 94 land cover types, which were developed based on more than 20 years of field investigations since 1980⁵⁹. The conversion from Olson to PFT categories is done within the code of ORCHIDEE based on cross-walking table. The PFT map based on Olson categories was provided by ORCHIDEE guidelines (<https://forge.ipsl.jussieu.fr/orchidee/wiki/Documentation/Ancillary>). The potential tree cover across the globe was derived from Bastin et al.⁵⁸. Bastin et al. developed a random forest machine-learning model to extrapolate tree cover measurements from protected areas to the globe using satellite-observed environmental conditions. Notably, the tree cover potential has been heavily debated, as it may be overestimated^{64–66}. Therefore, this forestation potential should be regarded as an upper limit for global current tree cover. In the forestation scenario (SCE), the forest increase from current to potential levels was assigned to different forest types using their observed present-day fraction (used in the CTL run) as the weighting factor. This allocation principle ensured that dominant forest type increased most substantially in the SCE run. In addition, different definition and classification methods of forest among data sources or overfit of the machine learning models might lead to less forest cover of the potential level than the current level in a small fraction of vegetated lands. In such cases, we assigned the forest cover in the SCE run as that in the CTL run, suggesting no afforestation attempts.

The coupled land-atmosphere model does not incorporate the ocean module, which help limit potential biases propagated from oceanic processes. To ensure accurate representation of conditions over the oceans, the model experiments were constrained by employing multi-model averaged sea surface temperatures (SSTs) and sea ice concentrations (SICs) from the CMIP6 1pctCO₂ simulations at 400 ppm. There are 41 ESMs providing the available outputs, including ACCESS-CM2, ACCESS-ESM1-5, CAMS-CSM1-0, CAS-ESM2-0, CESM2, CESM2-FV2, CESM2-WACCM, CESM2-WACCM-FV2, CIESM, CMCC-CM2-SR5, CanESM5, CanESM5-CanOE, CNRM-CM6-1, CNRM-CM6-1-HR, CNRM-ESM2-1, E3SM-1-0, EC-Earth3, EC-Earth3-AerChem, EC-Earth3-Veg, GOALS-f3-L, FGOALS-g3, FIO-ESM-2-0, GFDL-CM4, GFDL-ESM4, GISS-E2-1-H, HadGEM3-GC31-LL, HadGEM3-GC31-MM, INM-CM4-8, INM-CM5-0, IPSL-CM6A-LR, KIOST-ESM, MIROC-ES2L, MIROC6, MPI-ESM-1-2-HAM, MPI-ESM1-2-HR, MPI-ESM1-2-LR, MRI-ESM2-0, NESM3, NorCPM1, NorESM2-MM, UKESM1-0-LL.

We also conducted numerical experiments using another coupled land-atmosphere model, CESM version 2.0, to verify the robustness of our results. This model was developed by the National Center for Atmospheric Research (NCAR) with a spatial resolution of 1.9° × 2.5° (ref. 111). It employs the Community Atmosphere Model version 5 (CAM5) as its atmospheric component¹¹² and the Community Land Model version 4.0 (CLM4) as the land surface component¹¹³. Similarly, we set the CO₂ concentration at 400 ppm and used multi-model

averaged SSTs and SICs under this CO₂ concentration as boundary conditions. We conducted two 100-year equilibrium simulations with different PFT inputs: CTL (control) with current PFTs using Olson land cover map⁵⁹, and SCE (forestation scenario) with full-potential forestation PFTs based on Bastin et al.’s global potential tree cover map⁵⁸. Considering the required model spin-up time, we analyzed data from the last 60 simulation years. It is worth noting that while CESM-simulated runoff is significantly correlated with observations, CESM overall underperforms IPSL (Supplementary Fig. 26). We therefore present the CESM-based results in the Supplementary Information to support the robustness of our primary findings from IPSL.

Two sensitivity experiments with constrained forestation

As previously noted, the Bastin et al.’s data likely overestimate potential tree cover; thus, our full-potential forestation scenario (Bastin_Full) represents the upper bound of global forestation potential. In this regard, we designed two additional scenarios (Bastin_Refined_Climate and Bastin_Refined_Climate&Land) by progressively introducing more realistic constraints to test the robustness of our results. These three scenarios represent a range of possible forestation pathways, from the theoretical maximum to the most practical feasible.

Bastin_Refined_Climate builds upon Bastin_Full by excluding regions with frequent fires and where forestation would produce net warming due to reduced surface albedo. This refinement addresses two major critiques of the Bastin et al.’s dataset: overestimated potential in fire-prone grassland and savanna ecosystems, and the neglect of forestation-caused regional warming due to reduced albedo^{65,66}. Following Fesenmyer et al.⁶⁴, we used the 500 m MODIS Burned Area dataset to remove all non-cropland areas experiencing two or more fires during 2002–2022, assuming that such frequencies substantially limit tree density¹¹⁴. We further excluded regions where albedo-induced radiative warming exceeds the cooling from carbon sequestration of potential forestation, based on the dataset of Hasler et al.¹¹⁵. These constraints markedly reduce the estimated afforestation potential in tropical grassland and savanna ecosystems, particularly across Africa (Supplementary Fig. 1b).

Bastin_Refined_Climate&Land incorporated additional constraints on Bastin_Refined_Climate by excluding croplands, built-up areas, and wetlands to ensure land-use sustainability and feasibility. Urban and agricultural areas, given their essential roles in food production and human livelihoods, were masked out using the ESA CCI Global Land Cover dataset for 2000. Wetlands were excluded using the Global Lakes and Wetlands Database (GLWD, version 2) to prevent potential losses of large soil organic carbon (SOC) stocks following afforestation. Compared with the Bastin_Refined_Climate scenario, the further reduction in forestation potential in Bastin_Refined_Climate&Land predominantly occurs in cropland-dominated regions like Europe, African croplands, Southeast Asia, and eastern South America (Supplementary Fig. 1c).

Observed sensitivity of P-ET to forest cover change

To quantify the observation-based sensitivity of P-ET to forest cover change, we used precipitation data from the Multi-Source Weighted-Ensemble Precipitation (MSWEP; 1° × 1° resolution), ET data from the Global Land Evaporation Amsterdam Model (GLEAM; 0.1° × 0.1°), forest cover data from the European Space Agency Climate Change Initiative (ESA CCI; 30 m), near-surface air temperature from the Climatic Research Unit Time-Series (CRU TS; 0.5° × 0.5°), and incoming shortwave radiation from the Clouds and the Earth’s Radiant Energy System (CERES; 1° × 1°). Considering the role of mesoscale and large-scale circulation in redistributing atmospheric moisture, which can obscure the forest-precipitation signal, we analyzed 20-year means (2001–2020) rather than individual years. All datasets were resampled to a common 1° × 1° grid to match the coarser spatial resolution of model outputs.

For each vegetated grid cell, we performed regressions of precipitation (or ET) against forest cover, air temperature, and incoming shortwave radiation within a 3×3 window centred on the pixel, to estimate the sensitivity of precipitation (or ET) to forest cover change. The difference between precipitation and ET sensitivities represents the sensitivity of P-ET to forest cover changes, which approximates runoff responses over long-term scales. It is important to note that most observation-based space-for-time substitution approaches assume that forested and non-forested landscapes share similar atmospheric backgrounds, and thus cannot capture the influence of forest change on atmospheric circulation that redistributes moisture and affects precipitation. We hypothesize that this moisture redistribution effects of circulation diminishes the local forest-precipitation signal. Hence, we only selected pixels where precipitation and ET sensitivities to forest change were both statistically significant ($p < 0.05$), despite their limited number.

PET

In the climate models, PET is not directly available but can be calculated using model outputs of meteorological variables. To avoid the dependence of our results on the formulization of PET, we adopted two widely used versions of the Penman-Monteith model, including Penman-OW and PM-RC model. The Penman-OW model is a simplified version of the Penman-Monteith model, which is applied to open-water surface⁶⁷:

$$PET = \frac{s(R_n - G) + 6.43(1 + 0.536u)\gamma D}{\lambda(s + \gamma)} \quad (1)$$

The PM-RC model is another standardized version that is applicable to an idealized reference crop surface⁶⁸:

$$PET = \frac{0.408s(R_n - G) + \gamma \frac{900}{T+273} uD}{s + \gamma(1 + 0.34u)} \quad (2)$$

In these equations, s is the gradient of the saturation vapour pressure with respect to temperature (KPa K^{-1}), γ is the psychrometric constant ($0.0665 \text{ kPa K}^{-1}$), λ is the latent heat of vaporization (2.45 kJ kg^{-1}), T is the air temperature at 2 m above ground ($^{\circ}\text{C}$), u is the wind speed at 2 m height (m s^{-1}), D is the vapour pressure deficit (VPD) of the air at 2 m height as the difference between the saturation vapour pressure and the actual vapour pressure (kPa), $R_n - G$ is the net surface radiation minus the ground heat flux as the available energy ($\text{MJ m}^{-2} \text{ d}^{-1}$). The quantities s and D are computed according to

$$s = 4098e_s / (T + 273.3)^2 \quad (3)$$

$$D = e_s - e_a \quad (4)$$

$$e_s = 0.6108 \exp[17.27T / (T + 273.3)] \quad (5)$$

$$e_a = P_s \times SH / (0.378SH + 0.622) \quad (6)$$

where e_s is saturation vapour pressure (kPa) with respect to T , e_a and SH are the actual vapour pressure (kPa) and specific humidity (kg kg^{-1}) at 2 m height, respectively. P_s is the surface air pressure.

However, the Penman equation may overestimate PET because the underlying assumption of a saturated land surface is typically not satisfied. To address this issue, we also calculated PET using an energy-based approach proposed by Zhou and Yu^{116,117} (referred to as PET_e). PET_e represents the maximum ET constrained by the energy supply

(R_n) under conditions of saturated surface. PET_e is calculated using the net radiation (R_n) and the wet Bowen ratio (β_w), given by:

$$PET_e = \frac{R_n}{\lambda(1 + \beta_w)} \quad (7)$$

β_w is estimated based on the aerodynamics, that is, the ratio of sensible over latent heat exchanged between the saturated surface and the atmosphere, given by:

$$\beta_w = \frac{\gamma(T_s - T_a)}{e_s^* - e_a} \quad (8)$$

Where $T_s - T_a$ is the difference between surface (T_s) and air (T_a) temperatures, and $e_s^* - e_a$ is the difference in vapor pressure at the saturated surface (e_s^*) and of the air (e_a) above.

We noted for some grid cells, the PM-based and energy-based PET was smaller than the model-output ET, especially in energy-limited high latitudes. The potentially underestimated PET in such locations may lead to inaccurate n values as represented in the Budyko model. To address this issue, we replaced PET values with the ET values if the empirically calculated PET is less than ET.

Untangling the land surface effect and atmospheric effect with Budyko framework

The Budyko model assumes that precipitation partitioning at the surface is determined by climatic conditions and land surface characteristics under steady-state climatic conditions of the climatological (at least 30-year) scale water balance (i.e., $P = ET + R$)¹¹⁸. It should be noted that our equilibrium experiments meet this steady-state condition assumption. Within the Budyko framework, Climatic conditions refer to the precipitation and near-surface meteorological condition (i.e., PET), while land surface characteristics, such as vegetation, soil, land use and topographic factors, are encapsulated with a region-characteristic parameter n in Budyko models^{78,79}. Here, we adopted the Choudhury-Yang equation⁷⁹, a widely used Budyko model, to decompose the change in runoff caused by tree planting into contributions from the atmospheric changes and land surface changes. In this Budyko model, the fraction of evapotranspiration to precipitation (ET/P) is expressed as a function of the dryness index (PET/P) and the region-characteristic parameter (n):

$$\frac{ET}{P} = \left[\left(\frac{PET}{P} \right)^{-n} + 1 \right]^{-\frac{1}{n}} \quad (9)$$

Based on the global 60-year data of P , ET and PET , we first estimated the parameter n in each grid-cell by solving the above equation. Then we decomposed the changes in runoff (ΔR) as the sum of contributions from changes in P , PET and n by combining the first-order Taylor expansion of Choudhury-Yang equation and the water balance assumption:

$$\Delta R = \Delta P - \Delta ET = \left(1 - \frac{\partial ET}{\partial P} \right) \Delta P - \frac{\partial ET}{\partial PET} \Delta PET - \frac{\partial ET}{\partial n} \Delta n \quad (10)$$

where the three partial derivatives can be analytically derived from the Eq. (9), given by:

$$\frac{\partial ET}{\partial P} = \frac{ET}{P} \left(\frac{PET^n}{P^n + PET^n} \right) \quad (11)$$

$$\frac{\partial ET}{\partial PET} = \frac{ET}{PET} \left(\frac{P^n}{P^n + PET^n} \right) \quad (12)$$

$$\frac{\partial ET}{\partial n} = \frac{ET}{n} \left(\frac{\ln(P^n + PET^n)}{n} - \frac{P^n \ln P + PET^n \ln PET}{P^n + PET^n} \right) \quad (13)$$

In practice, calculating the above sensitivity coefficients using only 60-year data of either CTL or SCE may introduce some bias in the contributing components. Zhou et al.⁶¹ suggested that using the mean values of the sensitivity coefficients calculated by CTL and SCE data can best estimate the contributions of P, PET and n , given by:

$$\Delta R_p = -\frac{1}{2} \left[\left(\frac{\partial ET}{\partial P} \right)_1 + \left(\frac{\partial ET}{\partial P} \right)_2 - 2 \right] (P_2 - P_1) \quad (14)$$

$$\Delta R_{PET} = -\frac{1}{2} \left[\left(\frac{\partial ET}{\partial PET} \right)_1 + \left(\frac{\partial ET}{\partial PET} \right)_2 \right] (PET_2 - PET_1) \quad (15)$$

$$\Delta R_{land} = -\frac{1}{2} \left[\left(\frac{\partial ET}{\partial n} \right)_1 + \left(\frac{\partial ET}{\partial n} \right)_2 \right] (n_2 - n_1) \quad (16)$$

where the subscript 1 and 2 denote the 60-year period in CTL and SCE, respectively.

Then we can obtain the effect of forest-atmosphere feedbacks ($\Delta R_{atm} = \Delta R_p + \Delta R_{PET}$) and land surface changes (ΔR_{land}) on the estimated forestation-induced runoff changes.

Sensitivity tests of Budyko attribution

We first evaluated the robustness of our Budyko-based attribution analysis to different methods of estimating PET. The decomposition of runoff changes was repeated using outputs from the final 60 years of the equilibrium simulations with two Penman-type PET equations (Penman-OW and PM-RC) and an energy-balance-based PET (PETe). All three approaches yielded consistent attribution results, supporting our main conclusion that forest-atmosphere feedbacks dominate the latitudinally contrasting runoff responses to global forestation (Supplementary Fig. 10). This consistency is present despite the tendency of greater Penman-based PET than PETe particularly in arid regions (Supplementary Fig. 27), as also noted by Zhou and Yu^{116,117}. This PET difference has minor influence on our results (Supplementary Fig. 10) likely because potential forest expansion is mainly located in humid regions. Moreover, the Penman equations explicitly represent afforestation-induced increases in near-surface humidity and its suppression on atmospheric moisture demand – an effect that the energy-balance approach cannot fully capture (Supplementary Figs. 13a, c, e and 16). As the humidity-related effects are an important component of atmospheric feedbacks, our main analyses of runoff change decomposition are based on Penman-derived PET, while the results using PETe are presented in the Supplementary Information.

In addition to the use of 60-year equilibrium simulations, we further examined how climate variability across different timescales might affect the attribution of runoff responses. To this end, we implemented a bootstrap resampling approach to generate 1000 random year samples (with replacement from the final 60 years), for 30-, 40-, 50-, and 60-year timescales, respectively. For each sample, the forestation-induced runoff change was calculated as the difference between the SCE and CTL simulations and further decomposed into atmospheric feedback and land-surface components using the Budyko framework. The mean of the 1000 realizations represents the average runoff response for each timescale. The ensemble means derived from the 30-, 40-, 50-, and 60-year subsets produced results consistent with our main findings (Supplementary Fig. 9), indicating that internal climate variability has minimal influence on our conclusions.

Finally, we assessed the potential influence of forestation-induced changes in precipitation characteristics (e.g., rainfall intensity, snowfall

fraction) on the Budyko-based attribution of runoff changes. In cold regions, for example, a considerable portion of precipitation falls as snow during winter, and the subsequent spring or early-summer snowmelt substantially contributes to seasonal runoff. Since the standard Budyko framework only accounts for the first-order control of mean climate (precipitation and PET) and land surface conditions, the effects of precipitation characteristics on runoff (e.g., through the inter-seasonal processes) were implicitly conflated into the data-approximated n (ref. 69.). Hence, this may bias our interpretation of n changes as resulting from altered land surface properties. To address this bias, we adopted a modified Budyko-based approach for attribution following Zhou et al.⁶¹, which isolates the portion of precipitation change solely driven by altered precipitation characteristics (P^*). In this approach, the P^* -related portion of precipitation is artificially partitioned into runoff and directly subtracted from total precipitation and runoff, to present its effect being conflated into catchment properties (n) (Eq. 17). This method does not consider the potential effect of forestation-induced changes in land surface properties on runoff generation, implicitly assuming that runoff generation depends only on precipitation characteristics. Therefore, the ratio of the remaining runoff ($R_2 - P^*$) to the remaining precipitation ($P_2 - P^*$) in the forestation experiment is then assumed to be identical to that in the control simulation:

$$\frac{R_2 - P^*}{P_2 - P^*} = \frac{R_2'}{P_2'} = \frac{R_1}{P_1} \quad (17)$$

where subscripts 1 and 2 denote the CTL and SCE simulations, respectively, and subscript 2' suggests that the effect of precipitation characteristics (P^*) has been excluded for the forestation scenario. Solving for P^* yields:

$$P^* = \frac{R_2 \times P_1 - R_1 \times P_2}{P_1 - R_1} \quad (18)$$

Further, the effects of changes in the remaining precipitation (P_2), PET, and n on the remaining runoff (R_2) are decomposed under the Budyko framework. This allowed us to identify the more realistic climate change effect (changes in the mean P, PET and precipitation characteristics) and land surface effect on forestation-induced runoff changes:

$$\Delta R'_{atm} = -\frac{1}{2} \left[\left(\frac{\partial ET}{\partial P} \right)_1 + \left(\frac{\partial ET}{\partial P} \right)_2 - 2 \right] (P_2' - P_1) - \frac{1}{2} \left[\left(\frac{\partial ET}{\partial PET} \right)_1 + \left(\frac{\partial ET}{\partial PET} \right)_2 \right] (PET_2 - PET_1) + P^* \quad (19)$$

$$\Delta R_{land} = -\frac{1}{2} \left[\left(\frac{\partial ET}{\partial n} \right)_1 + \left(\frac{\partial ET}{\partial n} \right)_2 \right] (n_2' - n_1) \quad (20)$$

Together with the standard Budyko-based attribution, this extended approach, which explicitly accounts for precipitation characteristics, provides a refined estimate for the contributions of atmospheric feedbacks and land surface changes. Results from this sensitivity test remain consistent with our main findings, confirming that forest-atmosphere feedbacks predominantly drive the latitudinal contrast in runoff responses to global afforestation.

Moisture budget decomposition

To understand the mechanisms driving precipitation change, precipitation is decomposed into four components based on the vertical

integration of the moisture budget⁷¹:

$$P' = - \int_0^{P_s} [\bar{\nabla} \nabla q' + \bar{\omega} \frac{\partial q'}{\partial p}] \frac{dp}{g} - \int_0^{P_s} [\bar{\nabla} \nabla q] \frac{dp}{g} - \int_0^{P_s} [\omega' \frac{\partial q}{\partial p}] \frac{dp}{g} + E' + Res \quad (21)$$

Here the overbar operator $\bar{\cdot}$ denotes climatology in CTL and \prime represents the changes caused by global forestation (SCE-CTL). P , ω , q , $\bar{\nabla}$, E , P_s are precipitation, vertical pressure velocity, specific humidity, horizontal velocity, ET and surface pressure, respectively. The four main terms on the righthand side represent the thermodynamic effect associated with water vapour changes (ΔWV), altered horizontal moisture advection (ΔAdv) associated with horizontal wind changes, altered vertical dynamic effect ($\Delta Vert$) associated with vertical velocity changes, land surface ET changes (ΔET). The residual term (Res) is the precipitation change that is unexplained by above four processes, representing the impacts of transient eddies.

Global Budyko curve and global-scale surface parameter

We fitted the relationship between the evaporative index (ET/P) and the dryness index (PET/P) using global 60-year mean data (Supplementary Fig. 18). PET is the mean value of the two PET algorithms (Eqs. (1) and (2)). We binned the ET/P values according to their corresponding PET/P values. Following Ukkola et al.¹¹⁹, we determined the 5th and 95th percentile values of ET/P for each 0.1-wide PET/P bin. Then we fitted the Budyko curve and estimated the global-scale n value based on the global data with ET/P values falling between the 5th and 95th percentiles. The 5% and 95% thresholds were chosen to ensure that as much data as possible was used and to exclude outliers that could introduce bias into the fitted parameters. Apart from the fitted Budyko curve, we also plotted box plots with 0.2-wide PET/P bin in Fig. 2 to better demonstrate the impacts of global forestation on ET/P–PET/P relationship.

Data availability

All data used for our numerical simulations in this study are publicly available. The current PFT map based on Olson categories is available at (<https://forge.ipsl.jussieu.fr/orchidee/wiki/Documentation/Ancillary>). The dataset mapping the global tree restoration potential from Bastin et al. (<https://doi.org/10.1126/science.aax0848>) is available on request. The datasets mapping current SSTs and SICs are available at (<https://esgf-node.llnl.gov/projects/input4mips/>). The dataset mapping the net climate impact of afforestation while accounting for the albedo offset effect is available at <https://doi.org/10.7910/DVN/G17RXL>. The dataset mapping non-cropland areas that experienced two or more fires during 2002–2022 is available at <https://doi.org/10.6084/m9.figshare.27335799>. Global wetland datasets from the Global Lakes and Wetlands Database (GLWD) Version 2 are available at (<https://www.hydrosheds.org/products/glwd>). Global cropland and urban area datasets from the European Space Agency's Climate Change Initiative (ESA CCI) are available at (<https://maps.elie.ucl.ac.be/CCI/viewer/download.php>).

Code availability

Code and documentation for the IPSL model are publicly available at (<https://cmc.ipsl.fr/ipsl-climate-models/ipsl-cm5/>). Description and code relevant to CESM are freely available online at (<https://www.cesm.ucar.edu/models/cesm2>). Model outputs were processed using the software Matlab 2023a. The main MATLAB scripts are available at (<https://doi.org/10.6084/m9.figshare.30959648>). All figures were created by the authors using MATLAB and Adobe Illustrator under institutional academic licenses.

References

- Fankhauser, S. et al. The meaning of net zero and how to get it right. *Nat. Clim. Chang.* **12**, 15–21 (2022).

- Climate Change 2022: Impacts, Adaptation and Vulnerability. Contribution of Working Group II to the Sixth Assessment Report of the Intergovernmental Panel on Climate Change.* (2022).
- Canadell, J. G. & Raupach, M. R. Managing forests for climate change mitigation. *Science* **320**, 1456–1457 (2008).
- Lewis, S. L., Wheeler, C. E., Mitchard, E. T. A. & Koch, A. Restoring natural forests is the best way to remove atmospheric carbon. *Nature* **568**, 25–28 (2019).
- Griscom, B. W. et al. Natural climate solutions. *Proc. Natl. Acad. Sci. USA.* **114**, 11645–11650 (2017).
- Arora, V. K. & Montenegro, A. Small temperature benefits provided by realistic afforestation efforts. *Nat. Geosci.* **4**, 514–518 (2011).
- Windisch, M. G., Davin, E. L. & Seneviratne, S. I. Prioritizing forestation based on biogeochemical and local biogeophysical impacts. *Nat. Clim. Chang.* **11**, 867–871 (2021).
- Bonan, G. B. Forests and climate change: forcings, feedbacks, and the climate benefits of forests. *Science* **320**, 1444–1449 (2008).
- Kristensen, J. Å et al. Tree planting is no climate solution at northern high latitudes. *Nat. Geosci.* **17**, 1087–1092 (2024).
- Betts, R. A. Offset of the potential carbon sink from boreal forestation by decreases in surface albedo. *Nature* **408**, 187–190 (2000).
- Zhao, M. et al. Ecological restoration impact on total terrestrial water storage. *Nat. Sustain.* **4**, 56–62 (2020).
- Feng, X. et al. Revegetation in China's Loess Plateau is approaching sustainable water resource limits. *Nat. Clim. Change* **6**, 1019–1022 (2016).
- He, C. et al. Future global urban water scarcity and potential solutions. *Nat. Commun.* **12**, 4667 (2021).
- Oki, T. & Kanae, S. Global hydrological cycles and world water resources. *Science* **313**, 1068–1072 (2006).
- Mekonnen, M. M. & Hoekstra, A. Y. Four billion people facing severe water scarcity. *Sci. Adv.* **2**, e1500323 (2016).
- Bright, R. M., Zhao, K., Jackson, R. B. & Cherubini, F. Quantifying surface albedo and other direct biogeophysical climate forcings of forestry activities. *Glob. Change Biol.* **21**, 3246–3266 (2015).
- Peng, S.-S. et al. Afforestation in China cools local land surface temperature. *Proc. Natl. Acad. Sci. USA.* **111**, 2915–2919 (2014).
- Lee, X. et al. Observed increase in local cooling effect of deforestation at higher latitudes. *Nature* **479**, 384–387 (2011).
- Filoso, S., Bezerra, M. O., Weiss, K. C. B. & Palmer, M. A. Impacts of forest restoration on water yield: a systematic review. *PLoS ONE* **12**, e0183210 (2017).
- Zhang, L., Dawes, W. R. & Walker, G. R. Response of mean annual evapotranspiration to vegetation changes at catchment scale. *Water Resour. Res.* **37**, 701–708 (2001).
- Brown, A. E., Zhang, L., McMahon, T. A., Western, A. W. & Vertessy, R. A. A review of paired catchment studies for determining changes in water yield resulting from alterations in vegetation. *J. Hydrol.* **310**, 28–61 (2005).
- Farley, K. A., Jobbágy, E. G. & Jackson, R. B. Effects of afforestation on water yield: a global synthesis with implications for policy. *Glob. Change Biol.* **11**, 1565–1576 (2005).
- Zhang, M. & Wei, X. Deforestation, forestation, and water supply. *Science* **371**, 990–991 (2021).
- Jackson, R. B. et al. Trading water for carbon with biological carbon sequestration. *Science* **310**, 1944–1947 (2005).
- Huxman, T. E. et al. Ecohydrological implications of woody plant encroachment. *Ecology* **86**, 308–319 (2005).
- Zhou, G. et al. Global pattern for the effect of climate and land cover on water yield. *Nat. Commun.* **6**, 5918 (2015).
- Sun, G. et al. Potential water yield reduction due to forestation across China. *J. Hydrol.* **328**, 548–558 (2006).

28. Ceballos-Barbancho, A., Morán-Tejeda, E., Luengo-Ugidos, M. Á & Llorente-Pinto, J. M. Water resources and environmental change in a Mediterranean environment: The south-west sector of the Duero river basin (Spain). *J. Hydrol.* **351**, 126–138 (2008).
29. Buttle, J.M. & Metcalfe, R.A. Boreal forest disturbance and streamflow response, northeastern Ontario. *57*, 5–18 (2000).
30. Zhou, G. et al. Forest recovery and river discharge at the regional scale of Guangdong Province, China. *Water Resour. Res.* **46**, 2009WRO08829 (2010).
31. Wang, S., Fu, B.-J., He, C.-S., Sun, G. & Gao, G.-Y. A comparative analysis of forest cover and catchment water yield relationships in northern China. *For. Ecol. Manag.* **262**, 1189–1198 (2011).
32. Ellison, D., N. Futter, M. & Bishop, K. On the forest cover–water yield debate: from demand- to supply-side thinking. *Glob. Change Biol.* **18**, 806–820 (2012).
33. Cui, J. et al. Global water availability boosted by vegetation-driven changes in atmospheric moisture transport. *Nat. Geosci.* **15**, 982–988 (2022).
34. Spracklen, D. V., Arnold, S. R. & Taylor, C. M. Observations of increased tropical rainfall preceded by air passage over forests. *Nature* **489**, 282–285 (2012).
35. Yu, Y. et al. Observed positive vegetation-rainfall feedbacks in the Sahel dominated by a moisture recycling mechanism. *Nat. Commun.* **8**, 1873 (2017).
36. Staal, A. et al. Forest-rainfall cascades buffer against drought across the Amazon. *Nat. Clim. Change* **8**, 539–543 (2018).
37. Meier, R. et al. Empirical estimate of forestation-induced precipitation changes in Europe. *Nat. Geosci.* **14**, 473–478 (2021).
38. Link, A., Van Der Ent, R., Berger, M., Eisner, S. & Finkbeiner, M. The fate of land evaporation – a global dataset. *Earth Syst. Sci. Data* **12**, 1897–1912 (2020).
39. Laguë, M. M. & Swann, A. L. S. Progressive midlatitude afforestation: impacts on clouds, global energy transport, and precipitation. *J. Clim.* **29**, 5561–5573 (2016).
40. Li, Y. et al. Divergent hydrological response to large-scale afforestation and vegetation greening in China. *Sci. Adv.* **4**, eaar4182 (2018).
41. Nogherotto, R., Coppola, E., Giorgi, F. & Mariotti, L. Impact of Congo Basin deforestation on the African monsoon. *Atmos. Sci. Lett.* **14**, 45–51 (2013).
42. Yosef, G. et al. Large-scale semi-arid afforestation can enhance precipitation and carbon sequestration potential. *Sci. Rep.* **8**, 996 (2018).
43. Devaraju, N., Bala, G. & Modak, A. Effects of large-scale deforestation on precipitation in the monsoon regions: Remote versus local effects. *Proc. Natl. Acad. Sci. USA.* **112**, 3257–3262 (2015).
44. Portmann, R. et al. Global forestation and deforestation affect remote climate via adjusted atmosphere and ocean circulation. *Nat. Commun.* **13**, 5569 (2022).
45. Ma, S., Zhou, S., Yu, B. & Song, J. Deforestation-induced runoff changes dominated by forest-climate feedbacks. *Sci. Adv.* **10**, eadp3964 (2024).
46. Lejeune, Q., Davin, E. L., Guillod, B. P. & Seneviratne, S. I. Influence of Amazonian deforestation on the future evolution of regional surface fluxes, circulation, surface temperature and precipitation. *Clim. Dyn.* **44**, 2769–2786 (2015).
47. Su, Y. et al. Asymmetric influence of forest cover gain and loss on land surface temperature. *Nat. Clim. Chang.* **13**, 823–831 (2023).
48. Zhang, Y. et al. Asymmetric impacts of forest gain and loss on tropical land surface temperature. *Nat. Geosci.* **17**, 426–432 (2024).
49. De Hertog, S. J. et al. Effects of idealized land cover and land management changes on the atmospheric water cycle. *Earth Syst. Dyn.* **15**, 265–291 (2024).
50. Swann, A. L. S., Fung, I. Y. & Chiang, J. C. H. Mid-latitude afforestation shifts general circulation and tropical precipitation. *Proc. Natl. Acad. Sci. USA.* **109**, 712–716 (2012).
51. Duveiller, G., Hooker, J. & Cescatti, A. The mark of vegetation change on Earth’s surface energy balance. *Nat. Commun.* **9**, 679 (2018).
52. Roca, R. & Fiolleau, T. Extreme precipitation in the tropics is closely associated with long-lived convective systems. *Commun. Earth Environ.* **1**, 18 (2020).
53. Liu, C. Rainfall contributions from precipitation systems with different sizes, convective intensities, and durations over the tropics and subtropics. *J. Hydrometeorol.* **12**, 394–412 (2011).
54. Roca, R., Aublanc, J., Chambon, P., Fiolleau, T. & Viltard, N. Robust observational quantification of the contribution of mesoscale convective systems to rainfall in the tropics. *J. Climate* **27**, 4952–4958 (2014).
55. Tuinenburg, O. A., Theeuwes, J. J. E. & Staal, A. High-resolution global atmospheric moisture connections from evaporation to precipitation. *Earth Syst. Sci. Data* **12**, 3177–3188 (2020).
56. Dufresne, J.-L. et al. Climate change projections using the IPSL-CM5 Earth System Model: from CMIP3 to CMIP5. *Clim. Dyn.* **40**, 2123–2165 (2013).
57. Marti, O. et al. Key features of the IPSL ocean atmosphere model and its sensitivity to atmospheric resolution. *Clim. Dyn.* **34**, 1–26 (2010).
58. Bastin, J.-F. et al. The global tree restoration potential. *Science* **365**, 76–79 (2019).
59. Olson, D. M. et al. Terrestrial ecoregions of the world: a new map of life on Earth. *BioScience* **51**, 933 (2001).
60. Yang, H. et al. Changing the retention properties of catchments and their influence on runoff under climate change. *Environ. Res. Lett.* **13**, 094019 (2018).
61. Zhou, S., Yu, B., Lintner, B. R., Findell, K. L. & Zhang, Y. Projected increase in global runoff dominated by land surface changes. *Nat. Clim. Chang.* **13**, 442–449 (2023).
62. Yang, Y. et al. Evapotranspiration on a greening Earth. *Nat. Rev. Earth Environ.* **4**, 626–641 (2023).
63. Green, J. K. et al. Regionally strong feedbacks between the atmosphere and terrestrial biosphere. *Nat. Geosci.* **10**, 410–414 (2017).
64. Fesenmyer, K. A. et al. Addressing critiques refines global estimates of reforestation potential for climate change mitigation. *Nat. Commun.* **16**, 4572 (2025).
65. Veldman, J. W. et al. Comment on “The global tree restoration potential”. *Science* **366**, eaay7976 (2019).
66. Bond, W. J., Stevens, N., Midgley, G. F. & Lehmann, C. E. R. The trouble with trees: afforestation plans for Africa. *Trends Ecol. Evolution* **34**, 963–965 (2019).
67. Shuttleworth, W.J. et al. *Evaporation*. in *HANDBOOK OF HYDROLOGY* (McGraw-Hill Education, New York, 1993).
68. Allen, R. G., Pereira, L. S., Raes, D. & Smith, M. Crop Evapotranspiration: Guidelines for Computing Crop Water Requirements (FAO, 1998).
69. Padrón, R. S., Gudmundsson, L., Greve, P. & Seneviratne, S. I. Large-scale controls of the surface water balance over land: insights from a systematic review and meta-analysis. *Water Resour. Res.* **53**, 9659–9678 (2017).
70. Cui, J. et al. Vegetation forcing modulates global land monsoon and water resources in a CO₂-enriched climate. *Nat. Commun.* **11**, 5184 (2020).
71. Chou, C., Neelin, J. D., Chen, C.-A. & Tu, J.-Y. Evaluating the “rich-get-richer” mechanism in tropical precipitation change under global warming. *J. Clim.* **22**, 1982–2005 (2009).

72. Seager, R., Naik, N. & Vecchi, G. A. Thermodynamic and dynamic mechanisms for large-scale changes in the hydrological cycle in response to global warming*. *J. Clim.* **23**, 4651–4668 (2010).
73. Huang, P., Xie, S.-P., Hu, K., Huang, G. & Huang, R. Patterns of the seasonal response of tropical rainfall to global warming. *Nat. Geosci.* **6**, 357–361 (2013).
74. Liang, W. & Zhang, M. Summer and winter precipitation in East Asia scale with global warming at different rates. *Commun. Earth Environ.* **2**, 150 (2021).
75. Cuthbert, M. O., Rau, G. C., Ekström, M., O’Carroll, D. M. & Bates, A. J. Global climate-driven trade-offs between the water retention and cooling benefits of urban greening. *Nat. Commun.* **13**, 518 (2022).
76. Zhang, L., Potter, N., Hickel, K., Zhang, Y. & Shao, Q. Water balance modeling over variable time scales based on the Budyko framework – model development and testing. *J. Hydrol.* **360**, 117–131 (2008).
77. Gan, G., Liu, Y. & Sun, G. Understanding interactions among climate, water, and vegetation with the Budyko framework. *Earth-Sci. Rev.* **212**, 103451 (2021).
78. Zhang, L. et al. A rational function approach for estimating mean annual evapotranspiration. *Water Resour. Res.* **40**, 2003WR002710 (2004).
79. Yang, H., Yang, D., Lei, Z. & Sun, F. New analytical derivation of the mean annual water-energy balance equation. *Water Resour. Res.* **44**, 2007WR006135 (2008).
80. Zeng, Z. et al. Impact of Earth Greening on the Terrestrial Water Cycle. *J. Climate* **31**, 2633–2650 (2018).
81. PIELKE, R. A. Sr et al. An overview of regional land-use and land-cover impacts on rainfall. *Tellus B* **59**, 587–601 (2007).
82. Pielke, R. A. Sr. et al. Land use/land cover changes and climate: modeling analysis and observational evidence. *WIREs Clim. Change* **2**, 828–850 (2011).
83. Pielke, R. A., Mahmood, R. & McAlpine, C. Land’s complex role in climate change. *Phys. Today* **69**, 40–46 (2016).
84. National Research Council. Radiative Forcing of Climate Change: Expanding the Concept and Addressing Uncertainties (National Academies Press, 2005).
85. Kabat, P. et al. (eds) Vegetation, Water, Humans and the Climate: A New Perspective on an Interactive System (Springer, 2004).
86. Hoek, V. et al. Shifts in regional water availability due to global tree restoration. *Nat. Geosci.* **15**, 363–368 (2022).
87. Zan, B. et al. Spatiotemporal inequality in land water availability amplified by global tree restoration. *Nat. Water* **2**, 863–874 (2024).
88. Sun, W. et al. Northern hemisphere land monsoon precipitation increased by the green Sahara during Middle Holocene. *Geophys. Res. Lett.* **46**, 9870–9879 (2019).
89. Dallmeyer, A. & Claussen, M. The influence of land cover change in the Asian monsoon region on present-day and mid-Holocene climate. *Biogeosciences* **8**, 1499–1519 (2011).
90. Teo, H. C. et al. Large-scale reforestation can increase water yield and reduce drought risk for water-insecure regions in the ASIA-PACIFIC. *Glob. Change Biol.* **28**, 6385–6403 (2022).
91. te Wierik, S. A., Cammeraat, E. L. H., Gupta, J. & Artzy-Randrup, Y. A. Reviewing the Impact of Land Use and Land-Use Change on Moisture Recycling and Precipitation Patterns. *Water Resour. Res.* **57**, e2020WR029234 (2021).
92. Xu, X. et al. Deforestation triggering irreversible transition in Amazon hydrological cycle. *Environ. Res. Lett.* **17**, 034037 (2022).
93. Liang, Y., Xu, X. & Jia, G. Deforestation drives desiccation in Global monsoon region. *Earth’s Future* **10**, e2022EF002863 (2022).
94. Fan, Y., Miguez-Macho, G., Jobbágy, E. G., Jackson, R. B. & Otero-Casal, C. Hydrologic regulation of plant rooting depth. *Proc. Natl. Acad. Sci.* **114**, 10572–10577 (2017).
95. Yang, Y., Donohue, R. J. & McVicar, T. R. Global estimation of effective plant rooting depth: Implications for hydrological modeling. *Water Resour. Res.* **52**, 8260–8276 (2016).
96. Shao, R., Zhang, B. & He, X. Implementation of dynamic effective rooting depth in evapotranspiration model deepens understanding of evapotranspiration partitioning under soil moisture gradients in China. *Water Resour. Res.* **58**, e2022WR032962 (2022).
97. Tao, Z., Neil, E. & Si, B. Determining deep root water uptake patterns with tree age in the Chinese loess area. *Agric. Water Manag.* **249**, 106810 (2021).
98. Ray, D. K. et al. Impact of land use on Costa Rican tropical montane cloud forests: Sensitivity of orographic cloud formation to deforestation in the plains. *J. Geophys. Res.: Atm.* **111**, D0208 (2006).
99. Leite-Filho, A. T., Soares-Filho, B. S., Davis, J. L., Abrahão, G. M. & Börner, J. Deforestation reduces rainfall and agricultural revenues in the Brazilian Amazon. *Nat. Commun.* **12**, 2591 (2021).
100. Khanna, J., Medvigy, D., Fueglistaler, S. & Walko, R. Regional dry-season climate changes due to three decades of Amazonian deforestation. *Nat. Clim. Change* **7**, 200–204 (2017).
101. Garcia-Carreras, L. & Parker, D.J. How does local tropical deforestation affect rainfall?: deforestation and rainfall. *Geophys. Res. Lett.* **38**, n/a-n/a (2011).
102. Hossain, F. et al. Local-To-Regional Landscape Drivers of Extreme Weather and Climate: Implications for Water Infrastructure Resilience. *J. Hydrologic Eng.* **20**, 02515002 (2015).
103. Hourdin, F. et al. The LMDZ4 general circulation model: climate performance and sensitivity to parametrized physics with emphasis on tropical convection. *Clim. Dyn.* **27**, 787–813 (2006).
104. Li, Z.-X. Ensemble Atmospheric GCM Simulation of Climate Interannual Variability from 1979 to 1994. *J. Clim.* **12**, 986–1001 (1999).
105. Krinner, G. et al. A dynamic global vegetation model for studies of the coupled atmosphere-biosphere system. *Glob. Biogeochem. Cycles* **19**, 2003GB002199 (2005).
106. Lian, X. et al. Biophysical impacts of northern vegetation changes on seasonal warming patterns. *Nat. Commun.* **13**, 3925 (2022).
107. Zeng, Z. et al. Climate mitigation from vegetation biophysical feedbacks during the past three decades. *Nat. Clim. Change* **7**, 432–436 (2017).
108. Lian, X. et al. Partitioning global land evapotranspiration using CMIP5 models constrained by observations. *Nat. Clim. Change* **8**, 640–646 (2018).
109. Do, H. X., Gudmundsson, L., Leonard, M. & Westra, S. The Global Streamflow Indices and Metadata Archive (GSIM) – Part 1: The production of a daily streamflow archive and metadata. *Earth Syst. Sci. Data* **10**, 765–785 (2018).
110. Gudmundsson, L., Do, H. X., Leonard, M. & Westra, S. The Global Streamflow Indices and Metadata Archive (GSIM) – Part 2: Quality control, time-series indices and homogeneity assessment. *Earth Syst. Sci. Data* **10**, 787–804 (2018).
111. Hurrell, J. W. et al. The community earth system model: a framework for collaborative research. *Bull. Am. Meteorol. Soc.* **94**, 1339–1360 (2013).
112. Neale, A. R. et al. Description of the NCAR community atmosphere model (CAM 5.0). Tech. Rep. NCAR/TN-486+STR (National Center for Atmospheric Research, 2012).
113. Lawrence, D.M. et al. Parameterization improvements and functional and structural advances in Version 4 of the Community Land Model. *J. Adv. Model. Earth Syst.* **3**, M03001 (2011).
114. Staver, A. C., Archibald, S. & Levin, S. A. The global extent and determinants of savanna and forest as alternative biome states. *Science* **334**, 230–232 (2011).
115. Hasler, N. et al. Accounting for albedo change to identify climate-positive tree cover restoration. *Nat. Commun.* **15**, 2275 (2024).

116. Zhou, S. & Yu, B. Reconciling the discrepancy in projected global dryland expansion in a warming world. *Glob. Change Biol.* **31**, e70102 (2025).
117. Zhou, S. & Yu, B. Physical basis of the potential evapotranspiration and its estimation over land. *J. Hydrol.* **641**, 131825 (2024).
118. Xu, X., Liu, W., Scanlon, B. R., Zhang, L. & Pan, M. Local and global factors controlling water-energy balances within the Budyko framework. *Geophys. Res. Lett.* **40**, 6123–6129 (2013).
119. Ukkola, A. M. et al. Reduced streamflow in water-stressed climates consistent with CO₂ effects on vegetation. *Nat. Clim. Change* **6**, 75–78 (2016).

Acknowledgements

This study was supported by the National Natural Science Foundation of China (42588201) and the Second Tibetan Plateau Scientific Expedition and Research Program (2024QZKK0301). This work was also supported by the Peking University-BHP Carbon and Climate Wei-Ming Phd Scholars Program (Grant No. WM202411). The analysis and calculations were supported by High-performance Computing Platform of Peking University.

Author contributions

S.P. and X. Lian designed the research. F.K., H.X. and X. Li performed the simulation. F.K. performed the analysis. F.K. X. Lian and C.H. drafted the paper. F.K., X. Lian, H.X., S.T., J.C., C.H., M.S., X. Li and S.P. contributed to the interpretation of the results and to the text.

Competing interests

The authors declare no competing interests.

Additional information

Supplementary information The online version contains supplementary material available at <https://doi.org/10.1038/s41467-026-68945-9>.

Correspondence and requests for materials should be addressed to Xu Lian or Shilong Piao.

Peer review information *Nature Communications* thanks Akash Koppa, Roger A. Pielke Sr and the other anonymous reviewer(s) for their contribution to the peer review of this work. A peer review file is available.

Reprints and permissions information is available at <http://www.nature.com/reprints>

Publisher's note Springer Nature remains neutral with regard to jurisdictional claims in published maps and institutional affiliations.

Open Access This article is licensed under a Creative Commons Attribution-NonCommercial-NoDerivatives 4.0 International License, which permits any non-commercial use, sharing, distribution and reproduction in any medium or format, as long as you give appropriate credit to the original author(s) and the source, provide a link to the Creative Commons licence, and indicate if you modified the licensed material. You do not have permission under this licence to share adapted material derived from this article or parts of it. The images or other third party material in this article are included in the article's Creative Commons licence, unless indicated otherwise in a credit line to the material. If material is not included in the article's Creative Commons licence and your intended use is not permitted by statutory regulation or exceeds the permitted use, you will need to obtain permission directly from the copyright holder. To view a copy of this licence, visit <http://creativecommons.org/licenses/by-nc-nd/4.0/>.

© The Author(s) 2026